



University of  
Massachusetts  
Amherst

## Inversion of Marine Radar Imagery to Surface Realizations and Dual-Polarization Analysis

Item Type	Thesis (Open Access)
Authors	Paulsen, Brian
DOI	<a href="https://doi.org/10.7275/2171338">10.7275/2171338</a>
Download date	2026-04-13 02:46:48
Link to Item	<a href="https://hdl.handle.net/20.500.14394/47616">https://hdl.handle.net/20.500.14394/47616</a>

**INVERSION OF MARINE RADAR IMAGERY TO  
SURFACE REALIZATIONS AND DUAL-POLARIZATION  
ANALYSIS**

A Thesis Presented

by

BRIAN D. PAULSEN

Submitted to the Graduate School of the  
University of Massachusetts Amherst in partial fulfillment  
of the requirements for the degree of

MASTER OF SCIENCE IN ELECTRICAL AND COMPUTER ENGINEERING

September 2011

Electrical and Computer Engineering

**INVERSION OF MARINE RADAR IMAGERY TO  
SURFACE REALIZATIONS AND DUAL-POLARIZATION  
ANALYSIS**

A Thesis Presented

by

BRIAN D. PAULSEN

Approved as to style and content by:

---

Stephen J. Frasier, Chair

---

Paul R. Siqueira, Member

---

Patrick A. Kelly, Member

---

Christopher V. Hollot, Department Chair  
Electrical and Computer Engineering

## ACKNOWLEDGMENTS

Many people have helped me both personally and academically in completing a master's thesis. I want to thank Dr. Stephen Frasier for all of his guidance and help. Without his knowledge of ocean wave dynamics and radar imaging, this thesis would not have been written. I also want to thank Dr. Paul Siqueira for providing feedback and introducing me to MIRSL. I met some great people when first starting and I will always remember walking through the woods, measuring tree diameters, and becoming coated in chalk dust. I want to thank Dr. Patrick Kelly for providing suggestions for areas of my thesis and comments on what to improve. In addition, I want to thank Dr. Robert Jackson for his years of guidance, imparted knowledge, and recommendations. He has been a great help in the transition from the academic environment to establishing a professional career. Dr. Dennis Goeckel was also of great help and I want to thank him for his time. Lastly, I want to thank all the faculty and staff of the ECE department for their help from when I just started at UMass to today.

Family and friends have also had a great impact on helping me over the last few years. My parents have always been there for support. They have encouraged my interests and guided me since childhood. My sister has also been a great person to talk with and she has always looked out for me. She has always supported my decisions and encouraged exploration of new things and places.

MIRSL has been a great place to work, with everyone supporting one another and providing a friendly and fun work environment. In particular, Mandy has filled my life much joy, friendship, and love throughout the last two years. Her presence has

made graduate school a great experience for me. I had no idea how well things would turn out when deciding to enter graduate school in early 2009.

## ABSTRACT

# INVERSION OF MARINE RADAR IMAGERY TO SURFACE REALIZATIONS AND DUAL-POLARIZATION ANALYSIS

SEPTEMBER 2011

BRIAN D. PAULSEN

B.Sc., UNIVERSITY OF MASSACHUSETTS

M.S.E.C.E., UNIVERSITY OF MASSACHUSETTS AMHERST

Directed by: Professor Stephen J. Frasier

The ocean influences global weather patterns, stores and transports heat, and supports entire ecosystems. An area of interest is the relationship between the observed backscattered power received by a surface-based marine radar and the ocean surface topography. Current methods for obtaining surface elevation maps involve either in situ devices, which only provide point measurements, or an interferometric radar, which can be costly. During the late 1990's and early 2000's a radar was built at UMass, called the Focused Phased Array Imaging Radar II (FOPAIR II), and deployed at a several locations. A method is discussed to determine a transfer function between displacement and backscattered power for each of the range bins used by the radar and evaluate it's accuracy by applying the transfer function to separate data sets. In addition, it is known that horizontal polarized (H-Pol) backscatter exhibits a very different characteristic than vertical polarization (V-Pol). The horizontal polarization data exhibits less echo power except for intermittent bright spots, colloquially

called sea spikes”, that only briefly occur. Determining if there is correlation between these bright returns and a characteristic of the of the surface topography is investigated.

# TABLE OF CONTENTS

	Page
<b>ACKNOWLEDGMENTS</b> .....	<b>iii</b>
<b>ABSTRACT</b> .....	<b>v</b>
<b>LIST OF TABLES</b> .....	<b>ix</b>
<b>LIST OF FIGURES</b> .....	<b>x</b>
 <b>CHAPTER</b>	
<b>1. INTRODUCTION</b> .....	<b>1</b>
1.1 History and Motivation .....	1
1.2 Outline of Thesis .....	3
<b>2. THEORETICAL BACKGROUND</b> .....	<b>5</b>
2.1 Radar Operation .....	5
2.2 Radar backscatter mechanisms .....	9
2.3 Radar Imaging Mechanisms .....	11
2.4 Wave Dynamics and the Dispersion Relation .....	12
2.5 Ocean Wave Spectra .....	13
2.6 Horizontal Polarization spikes .....	15
<b>3. INVERSION TECHNIQUE</b> .....	<b>17</b>
3.1 Methods .....	17
3.1.1 Data Sets .....	17
3.1.2 Filtering about the Dispersion Relation .....	19
3.1.3 Formulation of a Modulation Transfer Function .....	21
3.1.4 Development of a Parameterized MTF .....	23
3.1.5 Methods for Evaluating MTF .....	25
3.2 Processed Images and Results .....	26

3.2.1	Coherence Spectrum .....	26
3.2.2	Dispersion Relation Filter .....	30
3.2.3	Sample Modulation Transfer Functions .....	32
3.2.4	Histograms of Displacement .....	36
3.2.5	Scatter Plots Obtained by a Applying MTF .....	41
3.2.6	Improved Results.....	44
3.2.7	Comparison with Phillips Spectrum.....	50
<b>4.</b>	<b>DUAL POLARIZATION ANALYSIS .....</b>	<b>51</b>
4.1	Hilbert Transform on Displacement and Wave Envelope.....	51
4.2	Sea Spike Analysis .....	56
<b>5.</b>	<b>CONCLUSIONS .....</b>	<b>66</b>
5.1	Application of a MTF .....	66
5.2	Sea Spike Locations .....	67
5.3	Areas of Future Work .....	67
 <b>APPENDICES</b>		
<b>A.</b>	<b>SAMPLE MODULATION TRANSFER FUNCTIONS FOR DIFFERENT RANGES.....</b>	<b>69</b>
<b>B.</b>	<b>DATA ALLOCATION IN ENVELOPE IMAGES .....</b>	<b>74</b>
 <b>BIBLIOGRAPHY .....</b>		
		<b>77</b>

## LIST OF TABLES

Table	Page
3.1 Moments of Displacements. ....	39
3.2 Error in empirical MTFs when varying dispersion filter. ....	48
3.3 Error in MTFs using improved dispersion filtering and averaged MTF as base for parameterizations. ....	49

## LIST OF FIGURES

Figure	Page
2.1 Geometry for correcting circular wave fronts. ....	7
2.2 Antenna array module. ....	8
2.3 Bragg Scattering courtesy of <a href="http://earth.esa.int/">http://earth.esa.int/</a> . ....	10
2.4 Turbulent plume causing non-bragg scattering [14]. ....	11
3.1 Ratio of velocity spectrum to displacement spectrum. ....	19
3.2 Wave number frequency spectrum obtained from power imagery. ....	21
3.3 NRCS at zero azimuth for all ranges, in meters. ....	22
3.4 Measured Displacement, in meters, at zero azimuth for all ranges, in meters. ....	23
3.5 Pierson-Moskowitz spectrum for peak at frequency of 0.12 Hz. ....	25
3.6 Phase Difference of coherence spectra from first half and second half of data. ....	28
3.7 Magnitude of Coherence Spectrum Between Power and Displacement. ....	29
3.8 Phase of Coherence Spectrum Between Power and Displacement. ....	29
3.9 Dispersion Relation Filter. ....	30
3.10 Dispersion Relation Smoothed Power. ....	31
3.11 Magnitude of empirical MTF at 167 m. ....	33
3.12 Phase of empirical MTF at 167 m. ....	33

3.13	Magnitude of empirical MTF at 167 m in blue and parameterized MTF in red. ....	35
3.14	Phase of empirical MTF at 167 m in blue and parameterized MTF in red. ....	35
3.15	Histogram of the measured displacement at 167 m. ....	37
3.16	Histogram of the estimated displacement using empirical MTF from (3.2) at 167 m. ....	38
3.17	Histogram of the estimated displacement using parameterized MTF but keeping phase response from (3.2) at 167 m. ....	39
3.18	Histogram of the parameterized MTF with constant phase response at 167 m. ....	40
3.19	Scatter plot of measured displacement and displacement from non-parameterized MTF at 167 m. Red line is line of best fit. ....	42
3.20	Scatter plot of measured displacement and displacement from parameterized MTF keeping empirical phase response at 167 m. Red line is line of best fit. ....	43
3.21	Scatter plot of measured displacement and displacement from parameterized MTF with constant phase response at 167 m. Red line is line of best fit. ....	44
3.22	Improved Dispersion Filter. ....	45
3.23	Averaged empirical MTF magnitude in red and parameterized MTF in blue. ....	46
3.24	Averaged empirical MTF phase in red and parameterized MTF in blue. ....	47
3.25	Scatter plot of measured displacement and displacement from Phillips spectrum keeping phase response of empirical MTF at 167 m. ....	50
4.1	Horizontal polarization NRCS imagery. ....	52
4.2	Phase of wave envelope for segments of a sinusoidal wave envelope profile. ....	53

4.3	Process for creating image of power distribution with respect to complex wave envelope characteristics 1-D. ....	54
4.4	Process for creating image of power distribution with respect to complex wave envelope characteristics 2-D. ....	55
4.5	Average wave envelope profile as a function of the phase of the complex envelope. ....	57
4.6	Average V-Pol backscattered power as a function of the phase of the complex wave envelope. ....	58
4.7	Average H-Pol backscattered power as a function of the phase of the complex wave envelope. ....	59
4.8	Average V-Pol velocity as a function of the phase of the complex wave envelope. ....	60
4.9	Average H-Pol velocity of the corresponding to the top 10 percent of power as a function of the phase of the complex wave envelope. ....	61
4.10	Average V-Pol power, in dB, mapped to complex wave envelope magnitude and phase. ....	62
4.11	Average H-Pol power, in dB, mapped to complex wave envelope magnitude and phase. ....	63
4.12	Average V-Pol velocity, in m/s, mapped to complex wave envelope magnitude and phase. ....	64
4.13	Average H-Pol velocity, in m/s, mapped to complex wave envelope magnitude and phase. ....	65
A.1	Magnitude of Transfer function for range of 152 m. ....	69
A.2	Angle of Transfer function for range of 152 m. ....	70
A.3	Magnitude of Transfer function for range of 174 m. ....	70
A.4	Angle of Transfer function for range of 174 m. ....	71
A.5	Magnitude of Transfer function for range of 195 m. ....	71
A.6	Angle of Transfer function for range of 195 m. ....	72

A.7	Magnitude of Transfer function for range of 215 m.....	72
A.8	Angle of Transfer function for range of 215 m. ....	73
B.1	Intensity plot of number of data points in each pixel of Figure 4.10.....	74
B.2	Intensity plot of number of data points in each pixel of Figure 4.11.....	75
B.3	Intensity plot of number of data points in each pixel of Figure 4.12.....	75
B.4	Intensity plot of number of data points in each pixel of Figure 4.13.....	76

# CHAPTER 1

## INTRODUCTION

### 1.1 History and Motivation

The ocean covers roughly 71% of the earth's surface. It influences global weather patterns, stores and transports heat, and supports entire ecosystems. As a result, it is important for researchers to understand as much as possible about the various processes that occur at the surface and below. Radar systems can be used to image the surface of the ocean and gain insight about ocean processes occurring at and below the surface. There have been numerous studies on radar imaging of the ocean, some of which present results that further our current understanding on the physics behind ocean surface and electromagnetic interactions. Other studies utilize the collected data to develop models for describing a measured process.

One area of interest is the relationship between the observed backscattered power received by a surface-based radar and the ocean surface topography. Current methods for obtaining surface elevation maps involve either *in situ* devices or an interferometric radar. *In situ* devices could take the form of pressure sensors below the surface, which record the instantaneous height of the water column, or devices on the surface, such as buoys and wave wires. However, pressure sensors only give coarse elevation measurements and surface measurement devices may be partially out of the water at times. In addition, they are only point measurement devices as opposed to a mapping device. On the other hand, an interferometric radar, properly designed, can provide fine resolution and substantially more accurate elevation measurements, but the cost and complexity of one is usually significantly higher than a conventional ma-

rine radar. Because of these problems, there is interest by the shipping, defense, and oceanographic communities to determine methods to relate the backscattered power received by a marine navigation radar to the ocean surface displacement. Applications include adaptive helm control and unmanned marine vessels.

During the late 1990's and early 2000's a radar was built at UMass, called the Focused Phased Array Imaging Radar II (FOPAIR II), and deployed at a few locations including New Bedford, MA and La Jolla, CA [2][4][8]. This is an X-band radar utilizing interferometric antennas to measure surface topography and sub-meter range resolution in certain operating modes. This radar can measure backscattered power, Doppler velocity, and interferometric displacement of the ocean surface over a  $24^\circ$  azimuthal sector. As a result of the combined collection of velocity or interferometric displacement and backscattered power data, it is possible to use the data collected from this instrument to develop a relation between surface displacement and power. Data from an earlier version of the radar, called FOPAIR, is also used in this thesis and provides dual polarization data of the ocean surface but not interferometric information.

A goal of this thesis is to determine a transfer function between displacement and backscattered power for each of the range bins used by the radar and evaluate it's accuracy by applying the transfer function to separate data sets. One study [9] discusses a technique to invert marine radar images into surface elevation plots, and confirmed their results through a combination of empirical data and simulated results. A separate study [13] used the method described in [9] to successfully invert radar imagery. The method used for this thesis is very similar to that used by these studies, which have already shown some success in inverting marine radar imagery. In addition, it will be desirable to evaluate the effects of varying conditions on the accuracy of the derived transfer function. This will help determine when the proposed method can be applied and under what conditions it starts to break down.

In addition, it is known that horizontal polarized (H-Pol) backscatter exhibits a very different characteristic than vertical polarization (V-Pol). The horizontal polarization data exhibits less echo power except for intermittent bright spots, colloquially called “sea spikes”, that only briefly occur. Sea spikes are an area of interest for naval applications. There is interest in being able to better characterize H-Pol sea clutter in order to be able to detect objects and potential threats when at sea. The backscatter mechanism for sea spikes is not well understood and several theories have been put forth to explain their presence. They are often associated with waves that are whitecapping, however it is known that sea spikes are also present from waves that are not whitecapping. Because sea spikes are often associated with steep wave features, having knowledge of where sea spikes preferentially occur on a wave profile is of interest. Determining if there is correlation between these bright returns and a characteristic of the of the surface topography is an additional goal of this thesis. Processing of the data is performed to determine what location and magnitude on the wave envelope sea spikes often occur.

## **1.2 Outline of Thesis**

Chapter 2 gives a brief description of the the basic operation of the FOPAIR instrument as well as describing ocean wave dynamics and scattering mechanisms. This chapter describes correction factors for the measurements of the radar and how images are created from an array detected of voltages (proportional to the received electric field). It progresses to describing mechanisms for obtaining contrast of ocean waves in the imagery and discusses models for ocean wave spectra.

Chapter 3 describes the inversion technique used for obtaining an estimate of displacement from power data. This chapter describes the data set and filtering used to reduce unwanted noise. A coherence spectrum between power and displacement is shown to establish a confidence in the development of a modulation transfer func-

tion. A section describes how a modulation transfer function is computed and how a parameterized function is fitted as a model. Lastly, histograms and scatter plots of displacement are shown to evaluate the effectiveness of the modulation transfer function.

Chapter 4 evaluates where sea spikes most often occur on the ocean wave envelope. It begins by describing a method used to determine where a pixel in the imagery is on the ocean wave envelope. This chapter progresses to describing the average wave envelope profile and where the power and velocity are maximum on this profile for both horizontal and vertical polarization. The data is further divided to account for the magnitude of the wave envelope and an evaluation is made regarding the location of sea spikes with regard to the envelope characteristics.

Chapter 5 summarizes the topics and conclusions of the thesis and suggests future work that could be done.

## CHAPTER 2

### THEORETICAL BACKGROUND

#### 2.1 Radar Operation

The data presented here comes from two different deployments of FOPAIR imaging radar. One deployment [8] was in 1996 at Duck, North Carolina. This radar utilizes a pair of phased-array antennas for receiving: one for horizontal polarization, and one for vertical polarization. Two transmit horns were used to illuminate the area of the ocean surface for each polarization. Each of the receiving arrays consists of 64 linear tapered slot antennas arranged in groups of 16 sealed modules as shown in Figure 2.2.

The radar operates in a pulse-compressed mode where it transmits a short chirp of known bandwidth and mixes a copy of it with the received echo. In order to obtain an image of the ocean surface, a pulse is transmitted and the echo signal is measured from the first element of the first antenna array. This procedure is repeated for each element in the first array and then performed on all the elements of the second array, creating two arrays of received voltages due to the echoes. Each array has values, that when transformed properly, represent an echo from a given range at a given azimuth. The process of taking one scan and capturing an image of the ocean surface takes approximately 0.64 ms, which is less than the decorrelation time of the ocean surface at X band. Each element's received echoes are mixed with the transmitted chirp, resulting in a range to frequency conversion and an FFT of a data series from one array element will arrange the data by range. Additionally, performing an FFT

along one range across all elements of an antenna will sort the data according to its angle of arrival.

A second deployment occurred in 2000 at Scripps Beach, La Jolla, CA [3] using a newer revision of the FOPAIR called FOPAIR II. This radar operated in a similar manner but had one vertically polarized transmit horn and two vertically polarized receive arrays placed one on top of the other with some distance between for the purpose of retrieving interferometric information from the surface of the ocean.

To obtain velocity imagery, two sequential complex images separated by nominally 2.5 ms are cross correlated. The phase of the cross-correlation provides information about the Doppler velocity of the surface. The complex values from the cross-correlation are accumulated for several images in order to reduce speckle due to fading. Using the phase of the averaged cross-correlation image along with (2.1), the velocity of each pixel is computed.

$$v(t) = \frac{\lambda_r}{2\sin(\theta_i)} \frac{\phi(t)}{2\pi\tau} \quad (2.1)$$

In this equation  $v(t)$  is the measured velocity,  $\lambda_r$  is the radar wave length,  $\theta_i$  is the incidence angle of the electromagnetic waves,  $\phi(t)$  is the measured phase of cross correlation between subsequent complex images, and  $\tau$  is the time lag between the two complex images.

Several corrections have must be made to the raw data before it is accurate. One correction is applied for unknown cable length delays between elements. This achieved in a two step process, one a coarse correction and a second being a finer correction. The coarse correction is used to correct for cable lengths that are longer than one wavelength. For this correction, the complex data from two adjacent array elements are cross-correlated giving a complex cross-spectrum. The phase is plotted, which should ideally be flat over frequency, but long cables will create a delay resulting in a phase progression with frequency. Determining the slope of the phase progression

and compensating for it results in a coarse correction for long cable delays. The second and finer correction for cable delays is done by taking the average phase between the complex data of adjacent elements and applying the the appropriate phase compensation. This is done by determining the phase progression as one goes down the 64 elements and applying additional phase compensation down the elements.

Another correction is made to correct for circular wave fronts impinging on the array, producing range migration effects. Using a Taylor series expansion of the equation for the distance from one element to an observation point, it can be shown that the phase along the elements of the array has a total of three components. The complex voltage at each element is given by (2.2) where  $k$  is the radar wavenumber and the other variables are shown in Figure 2.1.

$$v_0(t) = e^{jkR} e^{-jkx_i \sin(\theta)} e^{jkx_i^2/2R} \quad (2.2)$$

The first component is a constant that is due to the distance a scatterer is from the

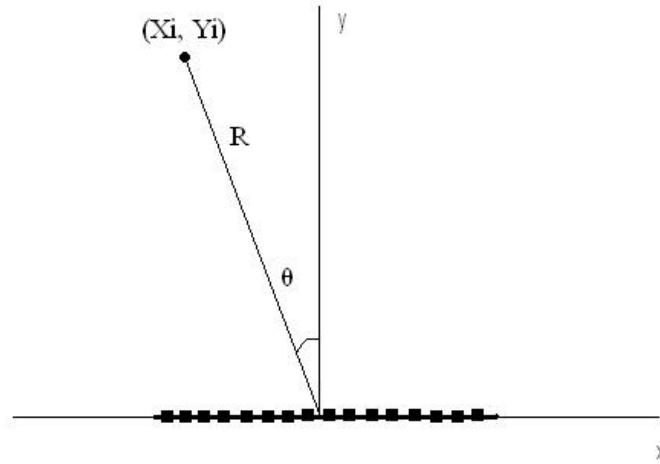


**Figure 2.1.** Geometry for correcting circular wave fronts.

array. The second component is a linear phase progression across the array which is

due to the angle of arrival. If the echo phase fronts followed a plane wave, then these two components would make up the entirety of the phase progression. However, since the scatterers are close to the antenna, a plane wave approximation cannot be made and a third, quadratic phase, term must be included.

For the radar data from the Scripps Beach deployment, it is capable of creating interferograms, phase differences between the top and bottom antenna that translate to displacement, in which a correction needs to be applied to account for small movements of the ocean surface in the time needed to sample both arrays sequentially. The phase variations in the interferograms have three components, one component is due to the look angle that is a constant phase progression in range. A second component is the phase change due to the topography of the ocean surface. The last component of phase in the interferograms is due to the movement of the ocean in the sample time between arrays. It is this component of phase that is corrected by using the velocity imagery that corresponds to the interferogram. The resulting corrected

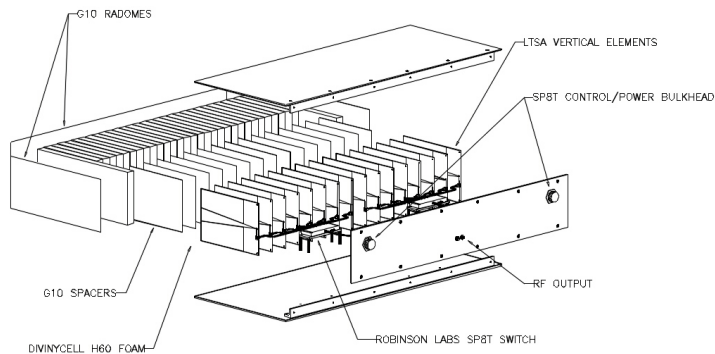


**Figure 2.2.** Antenna array module.

images can be processed and averaged to produce images of Doppler velocity, Doppler spectrum width, interferometric displacement, and estimated normalized radar cross section(NRCS).

## 2.2 Radar backscatter mechanisms

In order to understand and manipulate the data obtained from a radar imaging the ocean surface, it is necessary to be acquainted with ocean wave propagation characteristics and backscatter models. For vertical polarization and a moderately smooth surface, Bragg scattering of wind generated waves is the main backscatter mechanism. If the radar is observing the ocean at an incidence angle of  $\theta$  and operates at a radar wavelength of  $\lambda_r$ , then the Bragg resonant wavelength,  $\lambda_s$ , is defined by

$$\lambda_s = \frac{\lambda_r}{2} * \sin(\theta). \quad (2.3)$$

The Bragg resonance condition is illustrated in Figure 2.3. The combination of echoes from multiple wave fronts will add together in phase if the spacing between the waves projected in the direction of the radar follows (2.3). This in-phase addition of multiple echoes produces a large return signal. For the case of X-band radar, at near grazing angles, the Bragg resonant waves have a wavelength of approximately 1.5 cm, much shorter than ocean swells that are often tens or hundreds of centimeters in length. Hence, this model does not describe how the radar is able to image the surface, it only provides a mechanism for obtaining an echo from the surface, which, if otherwise was perfectly flat, would return no energy back to the radar at non-normal incidence angles.

Although Bragg scattering is considered to be the dominant backscattering mechanism in many conditions, there are situations in which the Bragg resonance mechanism breaks down and other scatter mechanisms appear dominant. Radar returns that are not consistent with Bragg scatter models are considered to be non-Bragg events. Frequently, non-Bragg scattering is associated with waves that are either breaking or have developed steep slopes on the forward face. In the case of a radar observing the nearshore zone, non-Bragg scattering will appear more frequently as the waves become steeper and approach breaking conditions. There have been many proposed

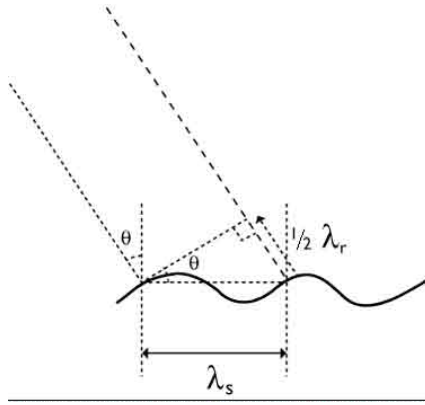


**Figure 2.3.** Bragg Scattering courtesy of <http://earth.esa.int/>.

backscatter mechanisms for non-Bragg events, however a comprehensive theory has not been established. One non-Bragg mechanism is proposed by Longuet-Higgins and Turner, and involves the formation of a turbulent plume as shown in Figure 2.4. In this model, a plume forms a rough cylinder on the rest of the wave and forms a sharp “toe” with the wave face. If the plume thickness is of the right dimensions so that surface roughness does not dominate and can provide reasonable backscatter, then this mechanism can provide substantial backscatter returns [14]. Others have proposed that as the front surface of a wave becomes steeper, a situation arises that allows for a single bounce specular reflection providing a high return echo. Still others have suggested that a double bounce return from a wave front, similar to a corner reflector, is the main non-Bragg mechanism. Many of these non-Bragg scatters are of most importance to horizontally polarized fields and are less prominent in vertically polarized data.

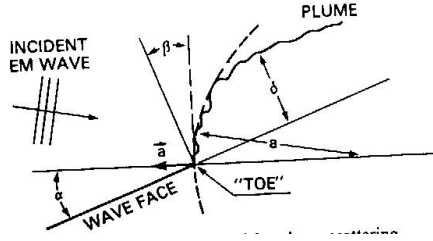


**Figure 2.4.** Turbulent plume causing non-bragg scattering [14].

## 2.3 Radar Imaging Mechanisms

The preceding section described mechanisms for obtaining a return from the ocean surface but these don't provide a means to see any detail in the ocean surface. As a result, Composite Surface Theory (CST) was developed to further expand on the imaging mechanism. CST describes the ocean surface as being composed of large swells, or gravity waves, on which smaller Bragg resonant waves ride on top of. Tilt modulation of the Bragg waves caused by the gravity waves results in a modulation in the back scattered power. When the gravity wave surface is tilted toward the radar, the backscattered power is generally larger. Depending on the grazing angle and wave heights, the echo from the side of the wave opposite of the radar will either have less echo or no echo. In addition, there are hydrodynamic modulations that strain and compress the Bragg resonant waves based on their location on the larger gravity wave. The straining or compression will shift the Bragg resonant frequency of the capillary waves and result in more or less backscattered power to the radar. Of course, as one approaches near grazing angles, there will be additional modulations such as shadowing due to waves blocking the line of sight to areas of the ocean surface. These three mechanisms are the primary means of obtaining contrast in the backscattered power imagery.

## 2.4 Wave Dynamics and the Dispersion Relation

The commonly accepted model for wave creation in deep water involves primarily wind induced waves. The wind blows over the surface of the water and creates small ripples. These ripples cause the surface to become rougher and causes more transfer of energy from the wind to the waves. Eventually, for a given wind speed over a long enough distance, the sea will reach a point where it is considered to be fully developed, meaning that the wave heights are a maximum for that wind speed. A particle of water will form an orbit as the wave passes by with little to no net movement. This orbit creates a Doppler shift when viewing with a radar and has a maximum at the peak of the ocean wave and a minimum at the trough. If one assumes sinusoidal waves propagating along the surface, the vertical and horizontal displacement of a particle in the wave from its equilibrium is given in (2.4) and (2.5), respectively

$$S_z = A \frac{\sinh(kz)}{\sinh(kh)} \sin(kx - \omega t) \quad (2.4)$$

$$S_x = A \frac{\cosh(kz)}{\sinh(kh)} \cos(kx - \omega t). \quad (2.5)$$

In the above,  $S_z$  is the vertical displacement,  $S_x$  is the the horizontal displacement in the direction of wave propagation,  $k$  is the wavenumber of the ocean wave, and  $\omega$  is the radian frequency of the ocean waves. Of course, true waves don't follow a pure sinusoidal movement, however, this is still a valid approximation in many cases. The measured velocity in V-Pol data has been shown to be a combination of the orbital velocity of the gravity waves, as described in the following paragraph, the surface current, and the mean Doppler shift due to both the incoming and receding Bragg waves. The phase velocity of Bragg resonant waves at near incident angles for a 10 GHz radar is approximately 23 cm/s. These effects on the Doppler velocity impact the measured velocity and must be accounted for in order to properly interpret the velocity.

Ocean waves can be modeled using the Navier-Stokes nonlinear differential equations for an incompressible fluid [1]. However the model can be simplified, if one assumes the surface displacement as sinusoidal in an incompressible medium with no vorticity and a zero mean current, then the wave propagation can be modeled by a relatively simple dispersion relation

$$\Omega = \sqrt{\left(gK + \frac{\tau_o}{\rho_o} K^3\right) \tanh(Kh)} \quad (2.6)$$

where  $\Omega$  is the wave angular frequency,  $g$  is the acceleration of gravity,  $K$  is the wave number of the ocean wave,  $\tau_o$  is the surface tension of the fluid,  $\rho_o$  is the fluid density, and  $h$  is the fluid depth. The dispersion relation relates the frequency at which the waves pass a given location with physical fluid parameters and size of the waves. The dispersion relation consists of two parts, one which describes capillary waves and one which describes gravity waves. Capillary waves are small wavelength waves typically defined as less than 1.7 cm whose main restorative force is due to surface tension. Gravity waves, on the other hand, are larger wavelength waves whose restorative force is due to gravity. For looking at gravity waves in deep water where the radar images, the dispersion relation can be simplified to  $\Omega = \sqrt{gK}$ . The phase velocity of these gravity waves is then  $V_p = \frac{\Omega}{K} = \sqrt{\frac{g}{K}}$ . Water particles in gravity waves will follow a nearly circular path with nearly no net movement. Since it is these gravity waves that are visible in the radar images, the gravity wave dispersion relation will be used as the model for the imaged waves. This model, however, breaks down when observing the surf zone or when wind speeds become so great that they cause whitecapping.

## 2.5 Ocean Wave Spectra

Not only are the propagation characteristics, defined by the dispersion relation, important to analyzing and processing ocean wave imagery, but the spectrum of the

ocean waves is also an important piece of information. The spectrum of the ocean wave displacement helps to determine the dominant wavelength and what range of wave frequencies are most prevalent in the radar imagery. Often the spectrum is affected by a few factors, such as the wind speed or the distance the wind blows over the open water, called the fetch. The length of time the wind has blown over the water and the depth of the water will also affect the evolution of the waves and resulting spectrum. If the wind has been blowing from a given direction for a sufficient time over a long fetch, the waves generated will reach their maximum and little energy from the wind will be transferred to the waves. When this occurs, the waves are considered to be fully developed. Models have been presented to approximate wave spectra for specific conditions, usually assuming a fully developed sea. Two models will be discussed in this section, one presented in 1958 by O.M. Phillips, and a second model by Pierson and Moskowitz presented in 1964 extends this model for lower frequency waves. A full discussion of ocean spectra for different conditions is discussed in [11].

In studying equilibrium conditions of ocean waves, Phillips observed a general form of the ocean wave spectra [10]. In his paper, Phillips describes that for a sea that has been well developed there is a range of higher frequencies that dominate in determining the ocean surface. In establishing the “equilibrium range”, Phillips shows that for a high enough wave number, the spectrum of the waves usually follows a curve given by,

$$S(\omega) = \frac{\alpha g^2}{\omega^5} \tag{2.7}$$

where  $S(\omega)$  is the dimensionless wave spectrum,  $\omega$  is radian frequency,  $\alpha$  is a constant, and  $g$  is the acceleration of gravity. However, (2.7) has only been shown to be valid for ocean wave frequencies that are somewhat larger. At low frequencies, it is not accurate as the function approaches infinity. Spectra collected on ocean waves show that the spectrum usually starts small for low frequencies and rises to a maximum before decaying away at higher frequencies. The spectrum described by Phillips

captures the behavior of the decay at high frequencies but becomes less accurate at low frequencies.

Pierson analyzed [12] the spectrum of fully developed waves obtained by Moskowitz for wind speeds ranging from 20 to 40 knots. In this work, Pierson compares his spectrum to the theories put forth by Phillips and others. He concluded that there must be more than just a  $\omega^{-5}$  dependence on frequency in the spectrum. Pierson notes that others have suggested an exponential term that depends on the frequency to multiply by the Phillips spectrum. This exponential term has the effect of acting like a high-pass filter and modifies the spectrum to better match the results from Moskowitz's data. Pierson developed Equation (2.8) to model the ocean wave spectra of fully developed seas,

$$S(\omega)d\omega = (\alpha g^2/\omega^5)e^{-\beta(\omega_0/\omega)^4}d\omega, \quad (2.8)$$

where  $S(\omega)$  is the dimensionless wave spectrum,  $\omega$  is radian frequency,  $\alpha$  is a dimensionless parameter that is typically equal to 0.0081,  $\beta$  is another dimensionless parameter that is typically equal to 0.74,  $g$  is the acceleration of gravity,  $\omega_0 = g/U$ , and  $U$  is the wind speed in m/s at 19.5 m above the ocean surface. In the Pierson-Moskowitz model,  $\omega_0$  can be thought of as the peak frequency in the spectrum. This model is still popular in describing wave spectra of waves on the ocean surface.

## 2.6 Horizontal Polarization spikes

In the vertical polarization imagery there is a fairly continuous modulation of power. In horizontal polarization, however, there is much less contrast among the waves and more intermittent bright targets that only briefly occur. Observers have noted that it often occurs with breaking waves, also known as whitecapping, but can also occur with just steep wave features [7][6]. The predominant scattering mechanism in horizontal polarization imagery is believed to be non-Bragg, and as a result the sea spikes observed in the data is not understood very well. In [7], it is described that the

sea spikes clearly evident in the H-Pol imagery are also present in the V-Pol imagery, but are less prominent due to the Bragg scattering that is prevalent in the V-Pol imagery. Essentially, the Bragg scattering dominates the backscattered power so that it is not evident from looking at the V-Pol imagery that a sea spike is present. Some involved in the detection of objects on the ocean surface are interested in these H-Pol spikes because the spikes cause complications in distinguishing between sea clutter and an object. This thesis attempts to correlate sea spikes with wave envelope features in order to better understand when they occur. This information can be used by others to improve the theory and models used for microwave scattering of the ocean surface.

## CHAPTER 3

### INVERSION TECHNIQUE

### 3.1 Methods

#### 3.1.1 Data Sets

As discussed in Section 2.1, results from data from two deployments of the FOPAIR radar are analyzed in this thesis. The data set from 1996 was taken in dual polarization with a 1.5 m range resolution from 150 m to 244 m. It images a  $24^0$  sector over the course of approximately 10 minutes. Post-processing, where correction factors are applied and beam-focusing and averaging to reduce the effects of fading are done, results in final images of backscatter power and Doppler velocity at a rate of 3 Hz.

The data set from the year 2000 deployment is not dual polarized but rather utilizes two receive antennas for the purpose of determining interferometric displacement of the waves. It images a  $30^0$  sector from a range of 36 m to 417 m with a 3 m range resolution. Post-processed images are set for a rate of 2.2 Hz over a 20 minute time frame. Ideally, the 2000 data set could establish a relationship between backscattered power and displacement. This deployment has direct measurements of the backscattered power and the phase change between two antennas, which can be linked to the ocean topography. The 1996 data set would then be most useful for investigating H-Pol sea spikes and their link to a given section of the ocean wave profile.

In establishing the validity of the interferometric displacement of the 2000 data set, a few tests are performed. It is accepted in the field that there is a close relationship between the measured Doppler velocity and displacement when using vertical polarization. One aspect of this relationship arises when looking at the coherence

spectrum between the velocity and displacement. The coherence spectrum,  $\Gamma(f)$ , is defined in equation (3.1) where \* means conjugation and  $V(f)$  and  $D(f)$  are the velocity and displacement spectrum, respectively

$$\Gamma(f) = \frac{\langle V(f)D(f)^* \rangle}{\sqrt{\langle V(f)V(f)^* \rangle \langle D(f)D(f)^* \rangle}}. \quad (3.1)$$

Ideally, the magnitude of the coherence spectrum should be close to unity. The angle between the two is expected to be close to zero due to how the radar measures Doppler velocity in vertical polarization. After the Bragg resonant velocity and mean current are subtracted from the velocity measurement, the component that remains is a measure of the orbital velocity of the gravity waves. Since the orbital velocity reaches a maximum at the peak of the waves and reaches a minimum at the trough, the displacement and velocity should be in phase. When checking this in the 2000 data set, the phase fell between  $+15^\circ$  and  $-60^\circ$  for frequencies less than 0.3 Hz, which is where the data is moderately correlated. This is a larger variation than desired and is not entirely conclusive in validating the displacement data.

Since the angle of coherence between velocity and displacement does not fully validate the results, a second test involving taking the ratio of the velocity and displacement in the frequency domain is performed. The ratio of  $V(f)/D(f)$  should result in a function that grows at a rate of  $f^2$ . This is due to the fact that the velocity spectrum decreases with increased frequency at a slower rate than the displacement by a factor of  $f^2$ . In taking the ratio of these two spectra on the 2000 data set, Figure 3.3 is obtained. The ratio of velocity and displacement from the 2000 data set does not match what is expected. Because the spectral relationship between the velocity and displacement does not match the expected results, the validity of the displacement data is uncertain. There are a number of corrections and processing that is done on the raw data to obtain final displacement images and it is possible that there is an error somewhere in that processing. The post-processing from raw

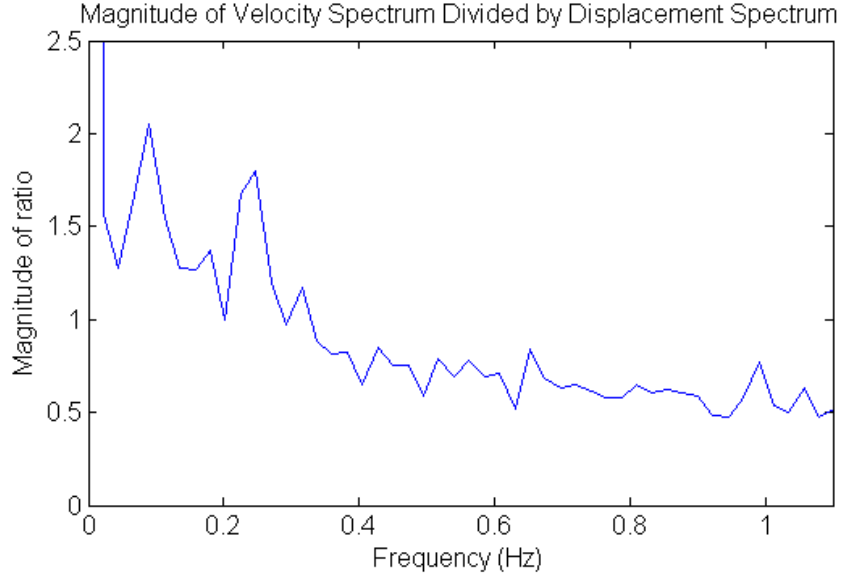


**Figure 3.1.** Ratio of velocity spectrum to displacement spectrum.

data to a series of corrected displacement images for the 2000 data set is done by code written and maintained by Gordon Farquharson. As a result, it is not possible at this time to further determine the discrepancy.

Due to the fact that some checks for validity of the 2000 data set did not agree with theory, the 1996 data set is instead used for creating a modulation transfer function. In order to create displacement imagery for a radar that has no interferometric measurements, velocity imagery is integrated. Although this method is not a precise measurement of the ocean surface displacement, it is generally accepted by the radar-oceanographic community that it yields reliable results [5].

### 3.1.2 Filtering about the Dispersion Relation

As discussed in Section 2.4 ocean gravity waves should closely follow the dispersion relation. In order to filter the data for power and displacement prior to creating a transfer function between power and displacement, the data is passed through a dispersion relation filter. To create a dispersion relation filter, an image of range verses time is needed since performing an FFT on this image will give frequency on

one axis and wavenumber on the other. The dispersion relation describes how these two quantities are related and is expected to be visible in this image. Using the V-Pol power imagery, the azimuth bin corresponding to broadside is selected and arranged as one column in a matrix where the row is the range index. This is done for 100 consecutive images for a total of 33 seconds or a matrix that is 64 x 100 representing range and time. A two-dimensional FFT is applied to the matrix, arranging the data by wavenumber and frequency. This process is repeated for each segment of 100 power images and ensemble averaged to yield an image showing where the power is distributed in frequency and wavenumber.

Figure 3.2 shows the image created by the process described above, along with a line in red that marks the equation for the dispersion relation for gravity waves that are advancing toward the radar. Wave numbers greater than zero in the image correspond to waves advancing toward the radar and wave numbers less than zero correspond to waves receding away from the radar. A threshold is applied to this image in order to create the filter that will be used later. The cutoff is set such that it is high enough to cut out most of the low level areas but not so high as to cut off the section of the image corresponding to receding waves, which have a weaker echo. The power associated with the receding waves is smaller in part because of tilt modulation. Because of tilt modulation, more power is received from the fronts of advancing waves than the backs of receding waves. Some of the backscattered power that does not lie near the dispersion relation may be due to non-Bragg scattering.

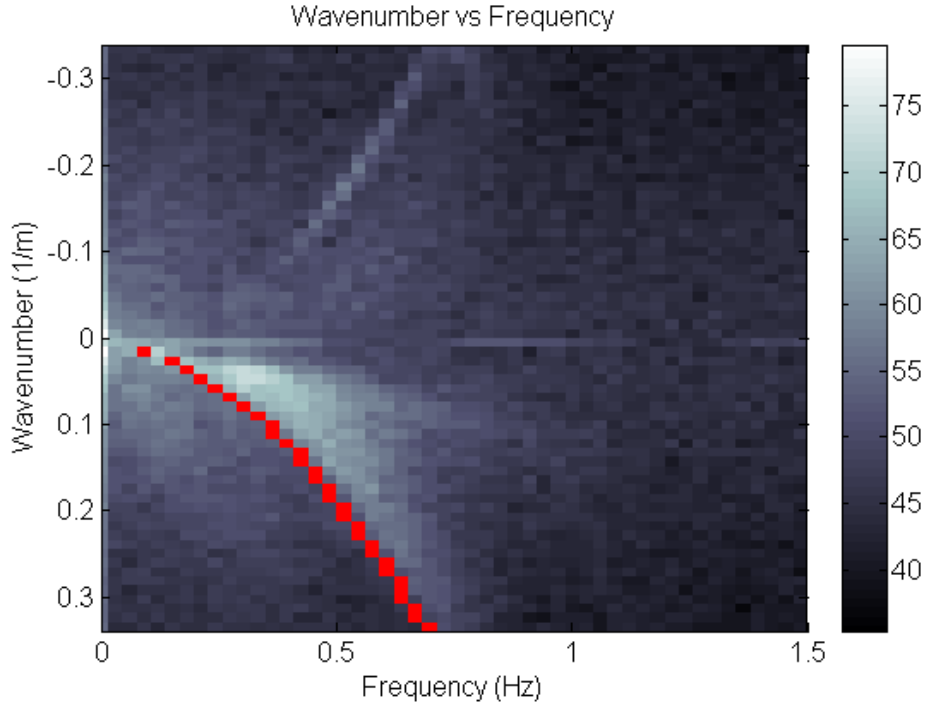


**Figure 3.2.** Wave number frequency spectrum obtained from power imagery.

### 3.1.3 Formulation of a Modulation Transfer Function

A modulation transfer function (MTF) is a function used to approximate how one can transform a backscattered power image into a surface realization. This is a function that is used for inverting the effects of all the modulations that occur in the forward model. Due to the questionable validity of the data set which measured interferometric displacement, the velocity from the 1996 data set is integrated and substituted as the displacement of the surface.

In order to create a MTF for the radar data, a time series of the displacement and backscattered power must be created for a given azimuth angle. For the results following, an azimuth angle of zero degrees (broadside) is selected. If this is done for all range bins, one obtains images given in figures 3.3 and 3.4. These are the same images used to create a dispersion relation filter except the horizontal axis is 33 seconds in length. From these two images, a particular range was taken to create

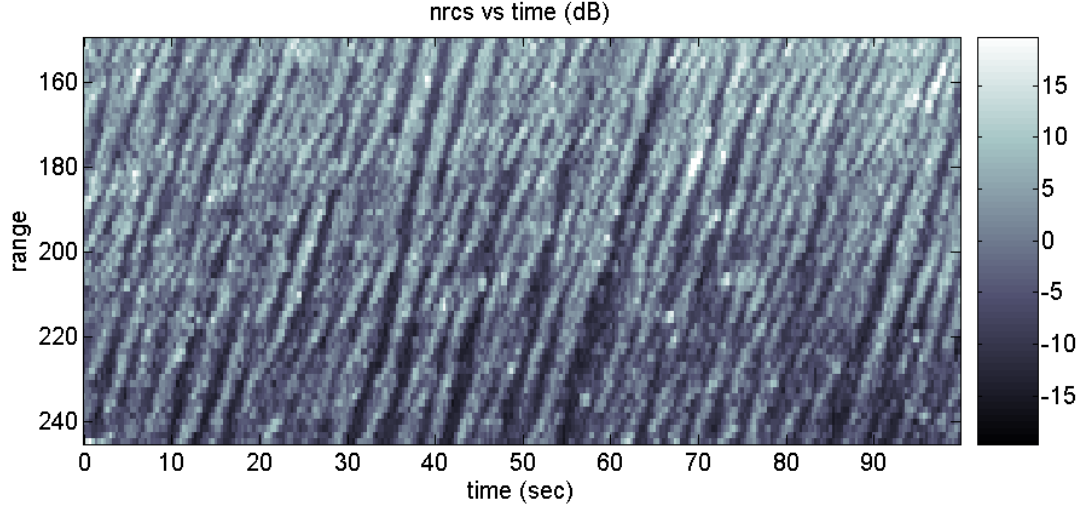


**Figure 3.3.** NRCS at zero azimuth for all ranges, in meters.

two time sequences, one of height and one of displacement. This time sequence is one horizontal row in figures 3.3 and 3.4. From time sequences like the ones shown but one third the length in time, a MTF is developed in a similar manner as how one would create a transfer function for a LTI system. A Fourier transform is taken of both sequences, sorting the data by frequency. If one names the Fourier transform of the power data and interferometric displacement data as  $P(f)$  and  $D(f)$ , respectively, then the MTF in the frequency domain is defined by (3.2),

$$H(f) = \frac{D(f)}{P(f)}, \quad (3.2)$$

where  $H(f)$  is the frequency domain representation of the MTF, which will be called the empirical MTF throughout this thesis. The empirical MTF is created by applying (3.2) to a 33 second time series and averaging the results with separate 33 second segments. Each of the 33 second segments of power and displacement are multiplied element by element with the dispersion relation filter prior to the application of (3.2) to create a MTF based on data that follows this relation. The MTF that is based on one 33 second segment of data is averaged with subsequent MTFs derived from

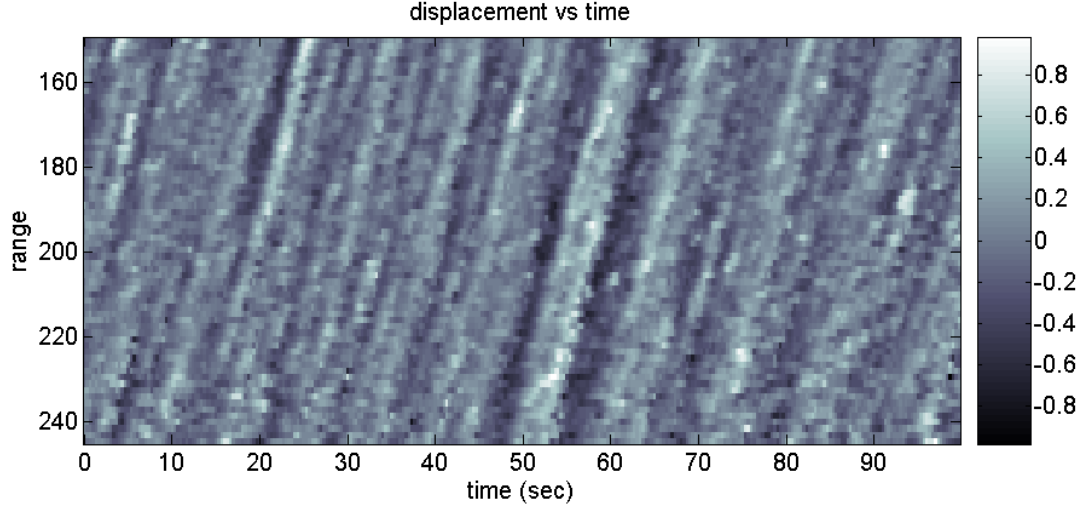


**Figure 3.4.** Measured Displacement, in meters, at zero azimuth for all ranges, in meters.

separate 33 second segments in the first half of the data set. This is the data that the MTF is trained upon and later the MTF is applied to the second half of the data set for evaluation. To obtain an estimate of the displacement, a time segment of the same range and from the second half of the data set is transformed into the frequency domain and multiplied with the MTF. This multiplication yields an approximate frequency domain representation of the surface displacement. This can be expressed mathematically as

$$Y_2(f) = H(f)P_2(f) \quad (3.3)$$

where  $P_2(F)$  is the Fourier transform of a separate power sequence and  $Y_2(f)$  is the Fourier transform of the estimated surface displacement. By performing an inverse FFT on  $Y_2(f)$ , an estimate of the surface displacement can be created.

### 3.1.4 Development of a Parameterized MTF

Developing a MTF in the way described in Section 3.1.3 allows for any arbitrary MTF. However, many times the MTF will follow a general shape that could be described by using a parameterized model. This would reduce the number of variables

that determine the shape of function and allow for a model that can be improved upon. By parameterizing the transfer function, it is hoped a more unified and predictable set of empirically determined MTFs can be established.

It is shown that ocean waves for fully developed seas often follow the Pierson-Moskowitz spectrum model. Because this spectrum is widely accepted and only has two parameters, it is used in formulating a parameterized MTF. To do this, an empirical MTF is created using the technique in Section 3.1.3 and the Pierson-Moskowitz spectrum is fitted to the magnitude of this data. A variation of the Pierson-Moskowitz spectrum is given by (3.4), where  $A$  is an a parameter based on the sea state,  $f$  is frequency in hertz, and  $f_0$  is the frequency at which the spectrum is at its maximum. Figure 3.5 shows an example of the Pierson-Moskowitz spectrum for  $f_0 = 0.12$  Hz and  $A = 7.05 \times 10^{-6}$ .

$$S(f) = (A/f^5)e^{-\frac{5}{4}(f_0/f)^4} \quad (3.4)$$

In this model,  $f_0$  can be quickly determined by having MATLAB determine the maximum element in the empirically determined MTF and convert that element value to the corresponding frequency that it represents. The value of  $f_0$  determines the dominant frequency in the spectrum. Once the value for  $f_0$  has been chosen, a loop iterates through values for  $A$  in the given model. The range of values over which the loop iterates was chosen by inspection of the empirical MTFs and values of  $A$  that will be able to replicate those curves. For each value of  $A$ , the root mean square error (RMSE) is evaluated between the parameterized function and the empirical MTF. An array containing the RMSE for each value of  $A$  is created and the minimum value in the array is chosen. The corresponding value of  $A$  is selected, finalizing the magnitude of the parameterized MTF.

In order to determine the phase of the parameterized MTF, one of two approaches is taken. One approach is to use the phase that is obtained from the empirical MTF without simplifying it. A second approach uses the observation that the phase is

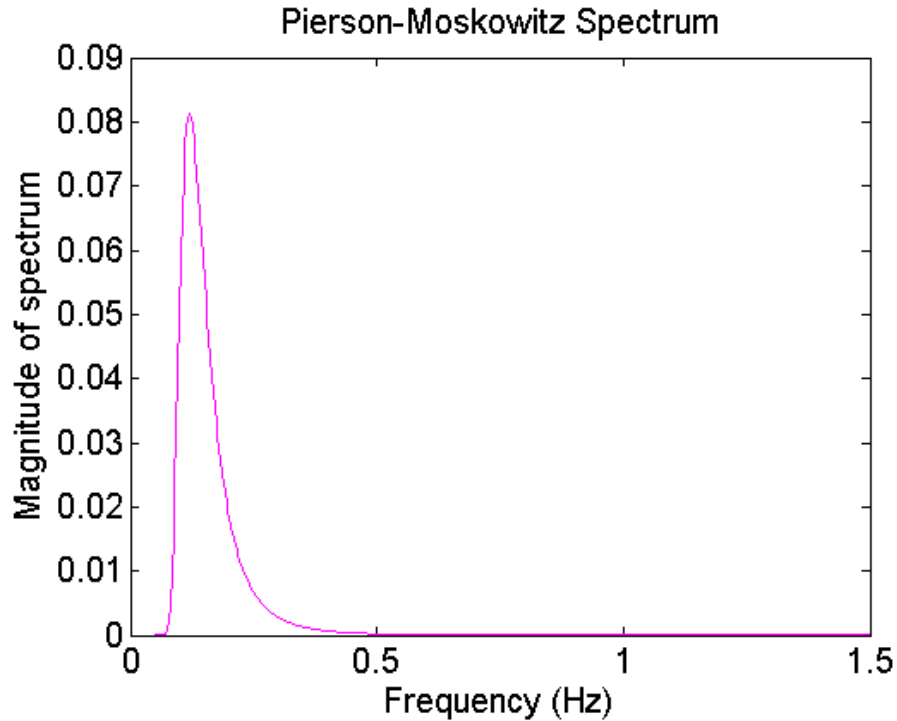


**Figure 3.5.** Pierson-Moskowitz spectrum for peak at frequency of 0.12 Hz.

mostly constant over the frequency range that the power and displacement have a high coherence. In this approach, the mean value of the phase over which the power and displacement spectrum are well correlated is set as the phase of the MTF. For negative frequencies, the mean value of the phase is multiplied by negative one for symmetry.

### 3.1.5 Methods for Evaluating MTF

Once a MTF has been created and filtered based on the first half of the data set, it is applied to the second half of the data set and evaluated on its effectiveness. A few methods are used to determine how well the estimate for displacement compares to the displacement derived from the velocity imagery. One method involves looking at the distribution of displacements obtained from the radar measurements and from using a MTF. In order to create distributions, the displacement sequence for the second half of the data is passed through a dispersion relation filter and loaded into

an array that keeps the time sequence of measured displacement. A separate array stores the results from applying the MTF and bringing the results back into the time domain. Histograms are created for each array using 100 divisions to present a distribution of the measured displacement and approximated displacement.

A second method for evaluating the results from applying a MTF is to create scatter plots of the measured displacement verses the estimated displacement. If the histograms match, it shows that the two displacement sequences share common statistics, however it does not say anything about how well the two trend together. It is possible to have two sequences have the same distributions but when one is reaching a maximum, the other one is not. By plotting a scatter plot of the two displacements, it can be determined whether the two trend together in time. Since the measured displacement and estimated displacement should result in the same numbers, the scatter plot should result in a line of points along a line with unity slope. In order to determine the slope of the line that best fits the data, a linear regression is performed. However, a simple linear regression is not appropriate for this situation due to the fact that there are measurement errors in both the measured displacement (derived from velocity) and estimated displacement. The appropriate regression to use is orthogonal linear regression, also known as total least squares regression. In this regression, the distance from each point directly to the line of regression is minimized as opposed to the standard regression where the vertical distance between each point and the line is minimized. The slope from the total least squares regression will provide a method to evaluate the performance of a MTF.

## **3.2 Processed Images and Results**

### **3.2.1 Coherence Spectrum**

One of the first steps toward ensuring that a MTF can be created between two data types involves correlating the two to make sure that there is some relationship

between the quantities. For this thesis, the coherence spectrum as defined in (3.5) is used to evaluate how well power and displacement are correlated for each frequency.  $P(f)$  and  $D(f)$  are the frequency domain representations of power and displacement, respectively.

$$\Gamma(f) = \frac{\langle P(f)D(f)^* \rangle}{\sqrt{\langle P(f)P(f)^* \rangle \langle D(f)D(f)^* \rangle}} \quad (3.5)$$

Plots of the coherence spectrum magnitude and phase averaged over the length of the 1996 V-Pol data set for a range of 166.5 m are shown in Figures 3.7 and 3.8, respectively. For frequencies less than about 0.5 Hz, the correlation is greater than 0.7, suggesting that there is a usable relationship between power and displacement at these frequencies. In addition, the phase plot is stable for the same frequency realm that there is a high coherence. This also suggests that there is a usable relationship for which a MTF can be developed. A coherence spectrum between the power and displacement of the first half of the data set also establishes a point of comparison for the displacement obtained through the use of a MTF. Since the MTF is based on the relationship between the power and displacement of the first half of the data set, it is not possible to get a coherence spectrum between the measured displacement and estimated displacement that is higher than the relationship the MTF is built upon. It can be useful to observe the coherence between the two quantities a MTF is based upon in order to better evaluate the results of the MTF.

A second area of concern is whether the relationship between power and displacement changes with time. For example, it is possible that the phase plot shown in Figure 3.8 changes to something very different if one is looking at one segment of the 1996 data set versus a different segment. If the phase plot changed, it would indicate that the relative phase of that frequency component is not the same as it was previously. In order to ensure that the phase relationship does not change over the course of data collection, the coherence spectra for the first half and second half of the data are computed. The difference in the phase of the two spectra is shown in Figure 3.6.

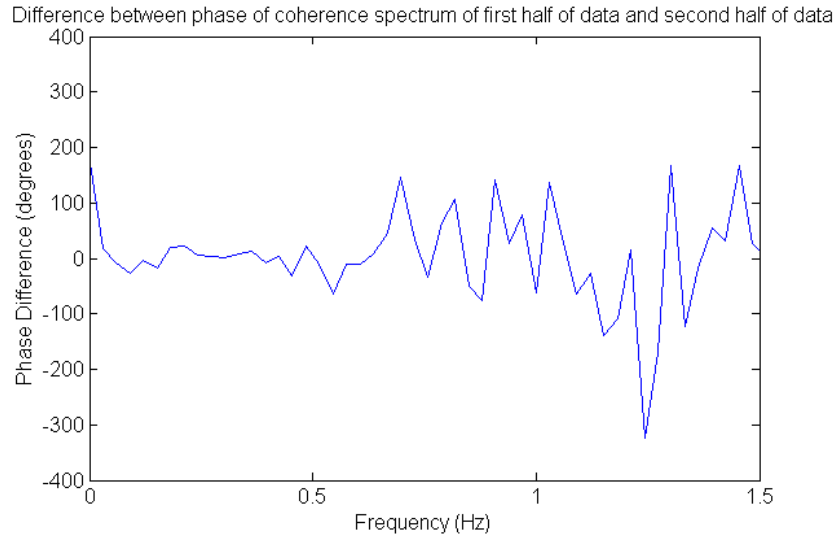


**Figure 3.6.** Phase Difference of coherence spectra from first half and second half of data.

The difference in the phases does not vary much from zero for frequencies below 0.5 Hz, indicating that there has not been a drastic delay for some frequencies. Further investigation into the first quarter and last quarter of the data set yielded similar results. If the phase plots had changed over the data collection time, it is likely that the results of an applied MTF would be similar to the measured displacement at first but then become increasingly different.

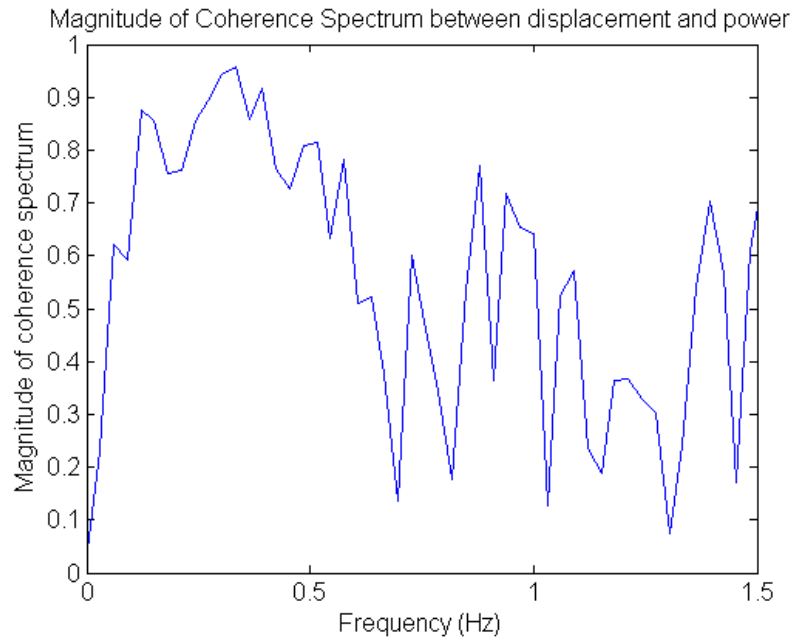


**Figure 3.7.** Magnitude of Coherence Spectrum Between Power and Displacement.

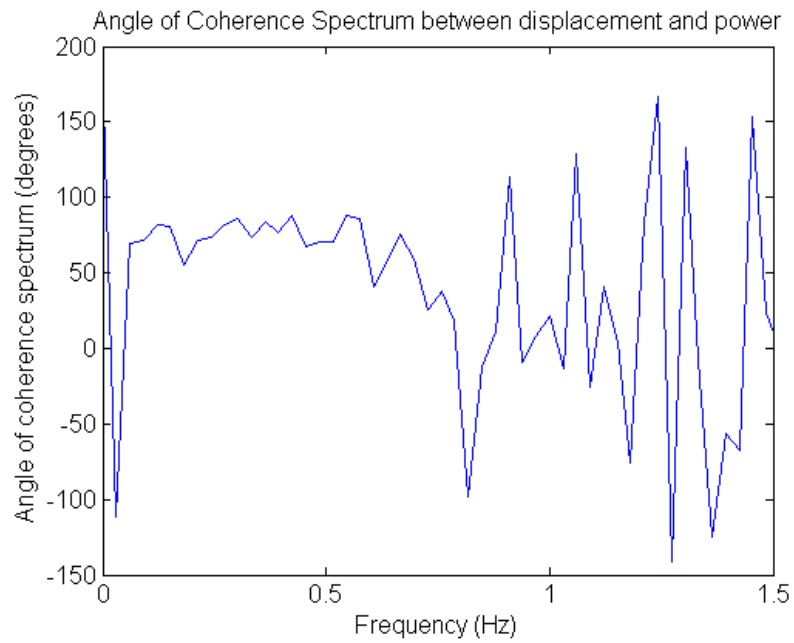


**Figure 3.8.** Phase of Coherence Spectrum Between Power and Displacement.

### 3.2.2 Dispersion Relation Filter

As discussed earlier in this thesis, filtering the V-Pol power and displacement is useful in removing some noise in order to emphasize the ocean gravity waves that are of interest. Figure 3.9 shows the filtering used. The white sections have a value of one and the black sections have a value of zero. This filter is multiplied element by element with the Fourier transformed power or displacement verses range images. Figure 3.9 is created by putting a threshold on the image described in Section 3.1.2. The threshold is set so that the receding gravity waves are still passed through but anything else that is lower in intensity than that is cut off. Although heavier filtering could have been used to try to reduce the low frequency and low wave number sections which are further from the dispersion curve. Heavier filtering is not used because it would have completely filtered out the receding gravity waves. Figure 3.10 shows the results of applying the dispersion relation filter to the V-Pol backscattered power imagery. In comparing with Figure 3.3 it is seen that the filtered image is smoother

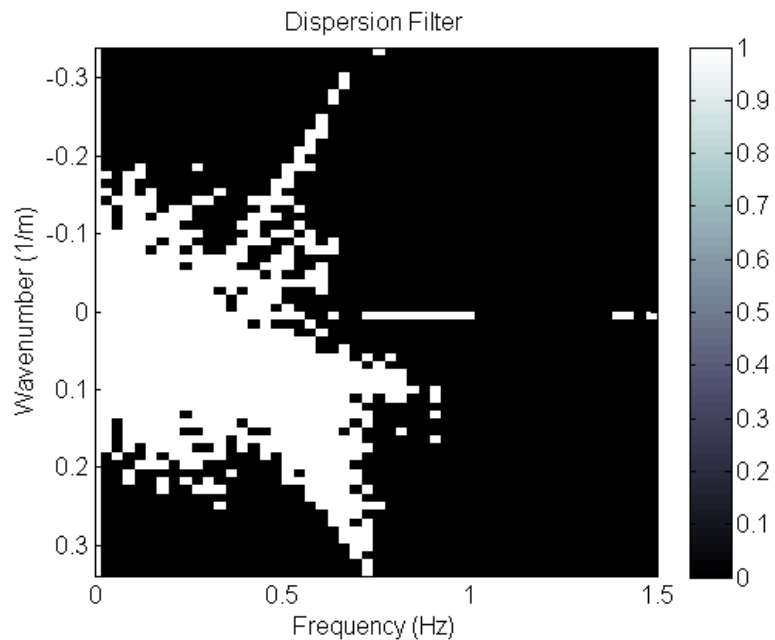


**Figure 3.9.** Dispersion Relation Filter.

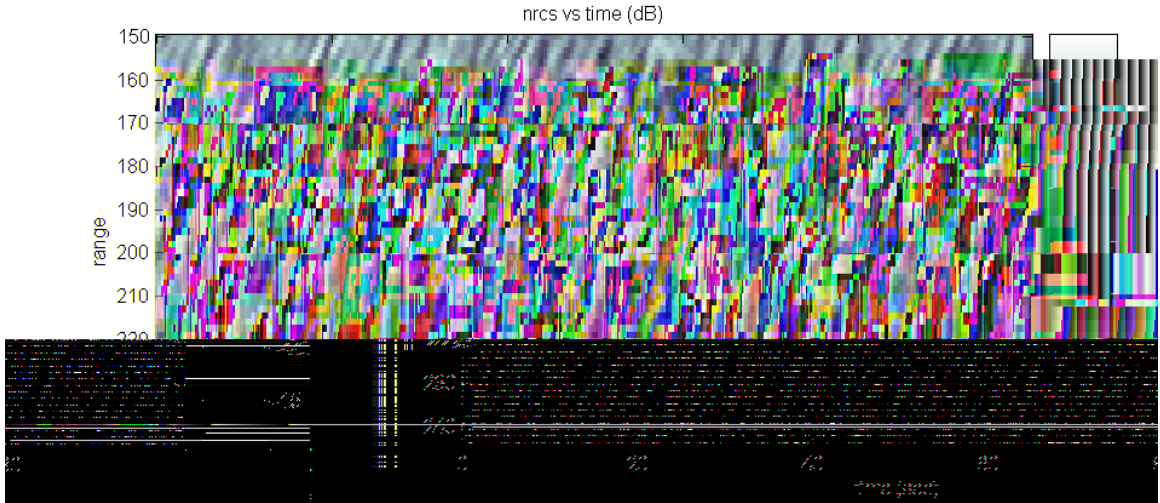


**Figure 3.10.** Dispersion Relation Smoothed Power.

as expected due to the filtering out of some high frequency noise components. It is this filtered data that the MTF will be based upon and compared with.

### 3.2.3 Sample Modulation Transfer Functions

A few methods are used to create a MTF, one of which is to simply use the empirically created MTF as described in Section 3.1.3. This is the basis for a parameterized MTF which attempts to best fit a function to the empirically created transfer function. A sample modulation transfer function for a pixel at broadside at a range of 166.5 m is shown in Figures 3.11 and 3.12. The validity of the MTF beyond 0.5 Hz is questionable since the coherence spectrum showed that the relationship between power and displacement have little correlation at these frequencies. The phase of the MTF varies some below 0.5 Hz but tends to stay between  $-50^\circ$  to  $-100^\circ$ . The relative stability of the phase indicates coherence of the relationship between the power and displacement for these frequencies. The spectrum as shown in Figure 3.11 has a similar shape to the Pierson-Moskowitz spectrum, shown in Figure 3.5, up to about 0.5 Hz. The similarity to the Pierson-Moskowitz spectrum suggests that a Pierson-Moskowitz model could be used in place of the spectrum to give reasonable results.

There is significant variation of the MTF shown if a different range bin is selected. Some samples of the empirical MTF derived for various ranges are shown in Appendix A. The somewhat large variation in MTF could be due to the limited time span of the data set. The entire data set is ten minutes long, of which only five minutes of data is used to create the MTF. The peak of the MTF is usually at a low frequency of about 0.1 Hz. With a frequency this low, little averaging is done in the course of five minutes used to create the MTF, hence the estimate error is higher.

Although it is possible to create and use the empirically created MTF, it is desirable to find a parameterized function that can be fit to the empirical MTF and still yield good results. For each empirical MTF, such as the one in Figures 3.11 and 3.12, a two parameter Pierson-Moskowitz spectrum is fit to the data up to 0.5 Hz in a least squares sense. By fitting the parameterized model to the empirical MTF, a plot

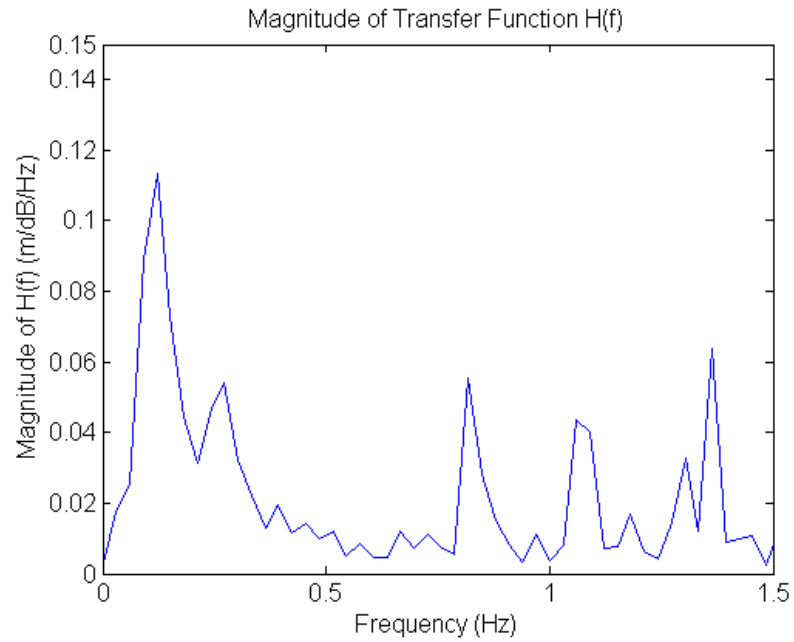


**Figure 3.11.** Magnitude of empirical MTF at 167 m.

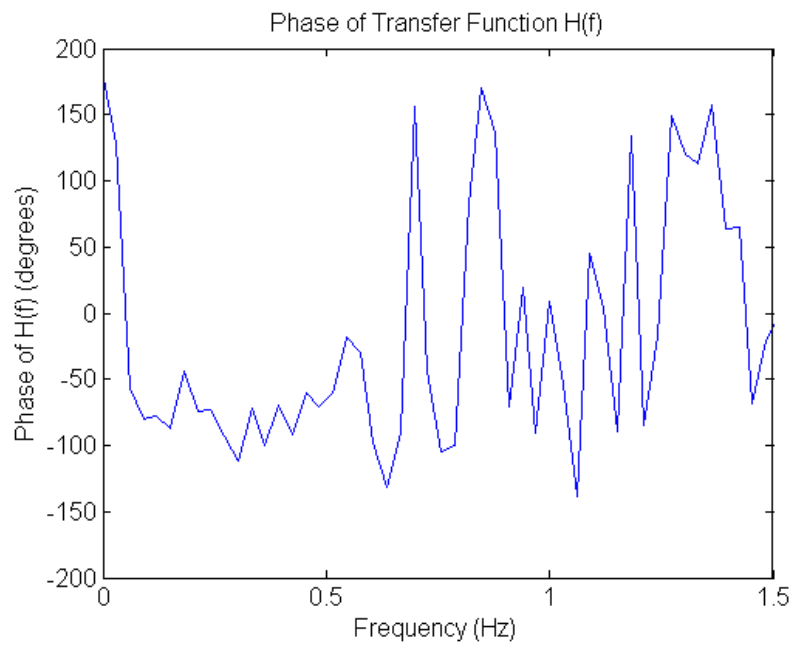


**Figure 3.12.** Phase of empirical MTF at 167 m.

shown in Figure 3.13 is obtained. In this plot the blue curve is the empirical MTF as obtained using (3.2) and the red curve is the parameterized Pierson-Moskowitz

spectrum curve fitted to the blue curve's data. The parameterized curve matches the empirical MTF quite well for frequencies below 0.5 Hz with the exception of a small peak around 0.3 Hz. The difference in results caused by not including the small peak as part of the spectrum is discussed in Section 3.2.5. A parameterization for the magnitude of the MTF can be obtained using the given model, but there is no established model for the phase of the MTF. As a result, two variations of the MTF phase response are utilized in this thesis. One variation of the phase response is to simply use the empirically created phase response along with the parameterized magnitude for the full MTF. Another method is based on observing that for frequencies less than 0.5 Hz, the frequency response is approximately flat. A line of zero slope is fitted for the constant phase section and combined with the parameterized magnitude to create the final MTF. An image showing an example of the fitted line to the phase response of the MTF is shown in Figure 3.14. In this thesis, results from using three types of MTFs are presented; one from (3.2), one from a parameterized magnitude for the MTF along with the phase response from (3.2), and lastly one from a parameterized magnitude for the MTF with a constant phase response.

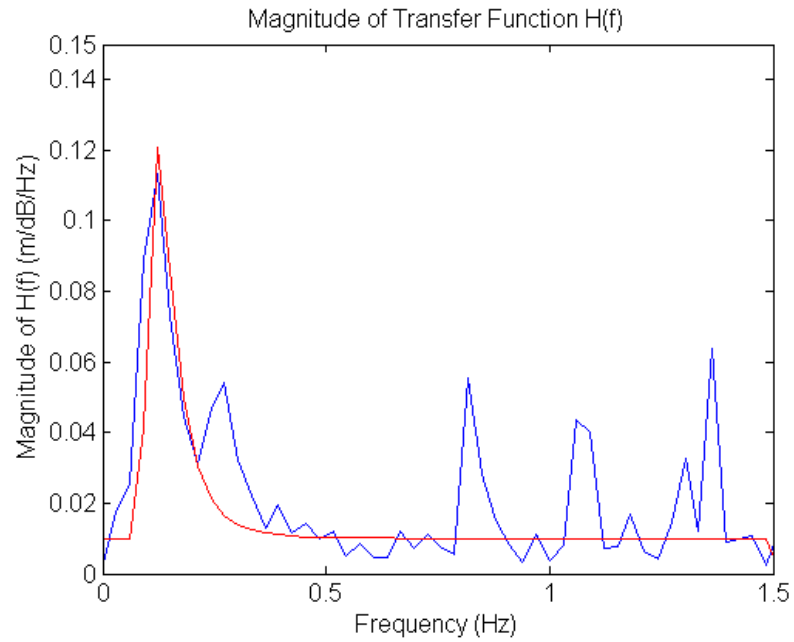


**Figure 3.13.** Magnitude of empirical MTF at 167 m in blue and parameterized MTF in red.

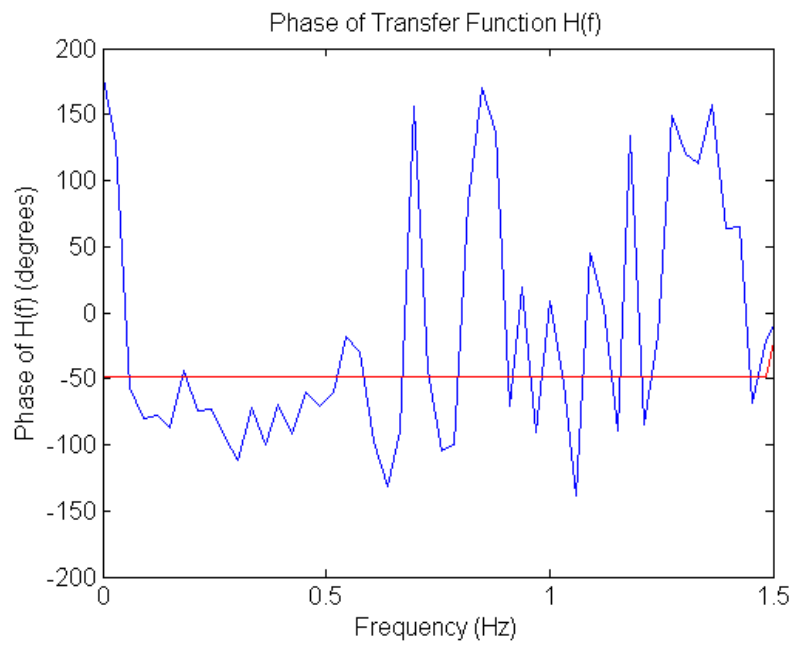


**Figure 3.14.** Phase of empirical MTF at 167 m in blue and parameterized MTF in red.

### 3.2.4 Histograms of Displacement

A first method for evaluating the displacement obtained from the application of a MTF is to observe the forms of the displacement histograms. A histogram of displacement shows the general distribution of displacements. If the MTF applied to the power data gives a distribution of displacements that is close to the distribution of measured displacements, then it is more likely that the MTF is yielding valid results. A stronger method of confirming the validity of the results of a MTF is to create a scatter plot, however using histograms can help establish the the statistical similarity between the estimated and measured displacement. The main histogram of which to compare others with is shown in Figure 3.15. This histogram plot displays the distribution of measured displacements for the second half of the data set at a range of 166.5 m. The processing to create the histogram plots incorporates filtering around the dispersion relation. The distribution of the measured displacements does not quite follow a normal distribution. The left side of the distribution rises more rapidly than the right side creating a slightly unbalanced distribution. A possible explanation for an uneven distribution is due to the displacement imagery being created from the velocity imagery. It is possible that there is some shadowing occurring, which would result in the velocity images not obtaining a good estimate in areas of lowest displacement.

Figure 3.16 shows the distribution of displacements obtained from applying a MTF created using (3.2), the empirical MTF, on the second half of the data set. This distribution is similar although it appears to rise more rapidly on the right side for positive displacements and taper off more gently for lower displacements. Figure 3.16 illustrates that the displacements obtained from this MTF over represent the negative displacements while slightly underestimate the positive displacements.

Figure 3.17 is the distribution of displacements for a parameterized MTF which keeps the empirical MTF phase response. The distribution for the displacements is

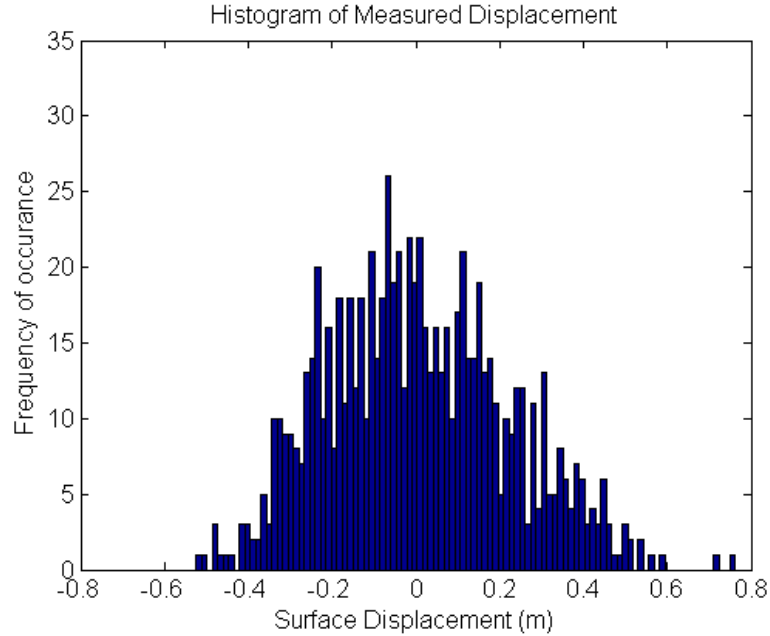


**Figure 3.15.** Histogram of the measured displacement at 167 m.

more Gaussian than previous histograms, likely due to the additional filtering effects of the rapidly decaying parameterized function in frequency. To some degree, the parameterized transfer function is acting like a low pass filter because it tends to decay faster than the empirical MTF. Figure 3.18 is a histogram plot of displacements when using a parameterized MTF with the constant phase response depicted in Figure 3.14. The distribution is again more Gaussian than the measured displacement distribution, however it has more weight on the positive displacements than the results in Figure 3.17. Since the two parameterized functions give distributions that don't have quite the same shape as the measured displacements, it is likely that they will not give surface realizations as accurate as the non-parameterized MTF.

Table 3.1 summarizes the mean and standard deviation of the displacements resulting from the application of each MTF. Each row describes the mean and standard deviation of the displacements obtained by applying a given MTF. The results in the table help supplement the distributions shown with a few defining numbers. The

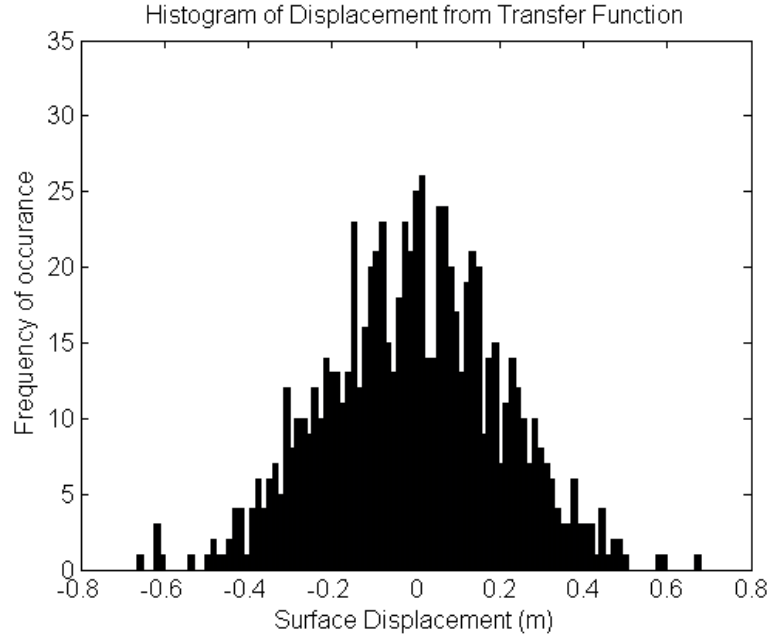


**Figure 3.16.** Histogram of the estimated displacement using empirical MTF from (3.2) at 167 m.

mean of all displacements is relatively small, however, there is some shift to one side of zero or the other side. The standard deviation of the displacements from the empirical MTF matches well with the standard deviation of the measured displacements. This is of importance since significant wave height, a measure of the sea state used in oceanography, is calculated as four times the value of the standard deviation of the wave displacement. The last two rows, corresponding to a parameterized MTF, have standard deviations close to the measured displacement, however they are not as good as the direct empirical MTF. In Section 3.2.5 it will become clear that the the empirical MTF yields more reliable results than the parameterized MTF, which is suggested by the results in this section.

Displacements	Mean Displacement (m)	Standard Deviation of Displacement (m)
Original Displacements	0.01	0.22
Displacements from Empirical MTF	-0.01	0.21
Displacements from Parameterized MTF keeping Original Phase	-0.03	0.19
Displacements from Parameterized MTF using Constant Phase	0.02	0.19

**Table 3.1.** Moments of Displacements.

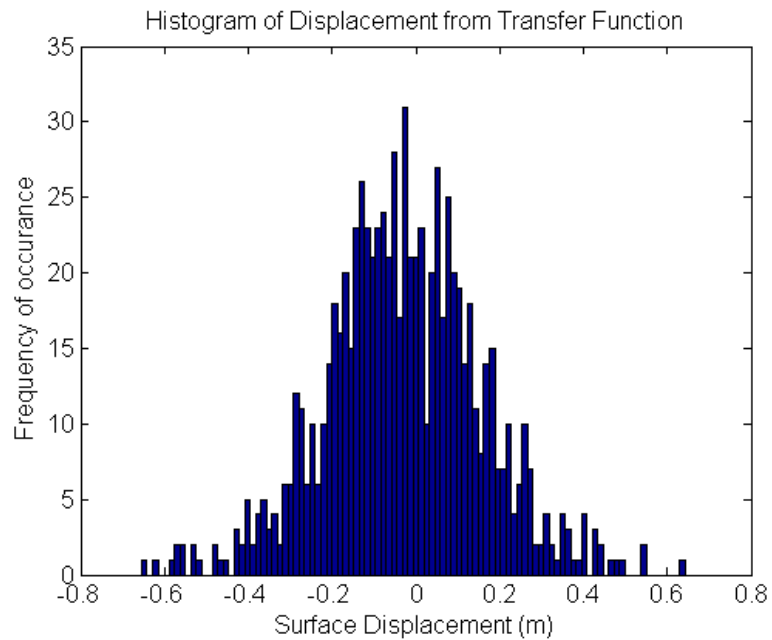


**Figure 3.17.** Histogram of the estimated displacement using parameterized MTF but keeping phase response from (3.2) at 167 m.

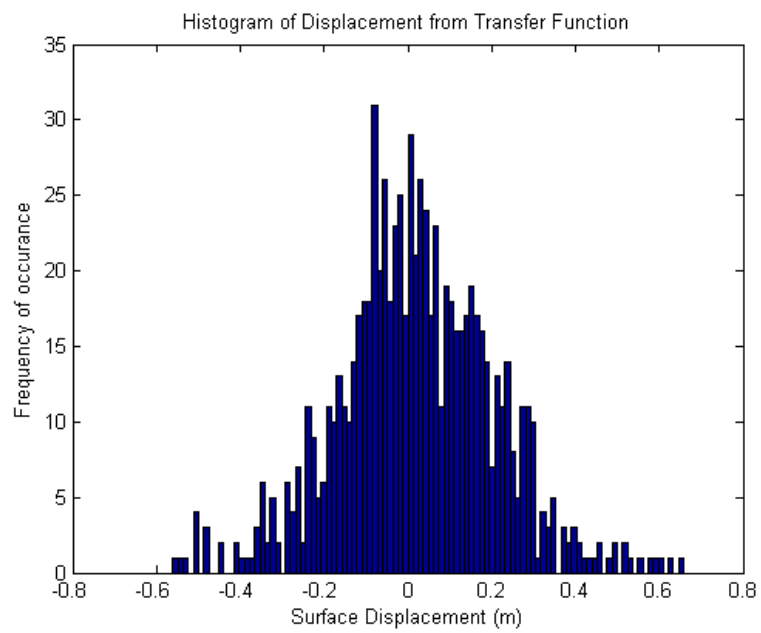


**Figure 3.18.** Histogram of the parameterized MTF with constant phase response at 167 m.

### 3.2.5 Scatter Plots Obtained by a Applying MTF

Although histograms can give important information about the statistical variation of the displacements, a perhaps more important method for evaluating the effectiveness involves creating a scatter plot of the displacements. The horizontal axis would represent the measured displacements and the vertical axis would represent the displacements resulting from applying one of the modulation transfer functions. The resulting plot should have the points forming a line with unity slope. With a slope of one, the displacement from the MTF matches up with the displacement that was measured at that instant in time. This is of course the ideal and in reality the slope may be slightly different. In addition, there will be some variation around the line of best fit. As described earlier in Section 3.1.5, orthogonal linear regression is used to create a line of best fit between the data points of the scatter plot.

Figures 3.19, 3.20, and 3.21 display the scatter plots obtained for each MTF case. The red line in each plot is a line of best fit whose equation is given in the lower right corner of the plot. In Figure 3.19, corresponding to the empirically created MTF, the scatter plot follows a line with a slope of 0.944, which is close to the desired slope of one. There is some variation around this line with most of the points falling between the line  $\pm 0.2$  m. When a parameterized MTF is applied which keeps the same phase response as the empirical MTF, a scatter plot shown in Figure 3.20 is obtained. The slope of the line is worse in with the parameterized MTF with a slope of 0.789. The amount of spread from the line of fit is still about the same as for the empirical MTF, suggesting a stable trend. However, when the phase response is approximated as a constant, as given in Figure 3.21, the spread becomes worse. In addition to the spread becoming worse, the slope further deviates away from one to a value of 0.745.

The main reason that there is a significant decrease in validity of the results from the parameterized MTFs, as compared to the empirical MTF, can be observed in Figure 3.13. The red parameterized MTF decays quickly and completely misses a

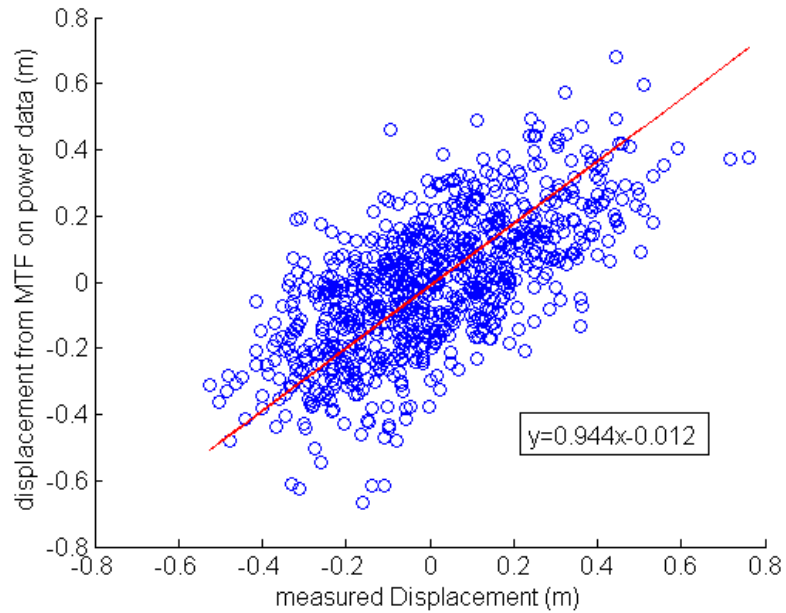


**Figure 3.19.** Scatter plot of measured displacement and displacement from non-parameterized MTF at 167 m. Red line is line of best fit.

small peak in the blue empirical MTF. Since this peak occurs where there is high coherence between the power and displacement, it needs to be included in the MTF in order to get better results. The results get worse for the case of a constant phase MTF because not only is there some information cut out of the magnitude plot, but there is an approximation made on the phase. The true phase response is not exactly flat and the approximation made introduces further error in the results.

The parameterized function is based on a spectrum that is itself a model. The conditions for developing the model were based on results obtained at a certain location in conditions where the sea was fully developed and the wind speed was between 10 m/s and 20 m/s. It is very likely that the sea was not fully developed when the data was collected by the FOPAIR instrument. In addition, the deployment was not far from the shore, which can result in refraction and reflections of the ocean waves. Because the conditions under which the data used for this thesis may have been different from those under which Pierson-Moskowitz spectrum is based, it is

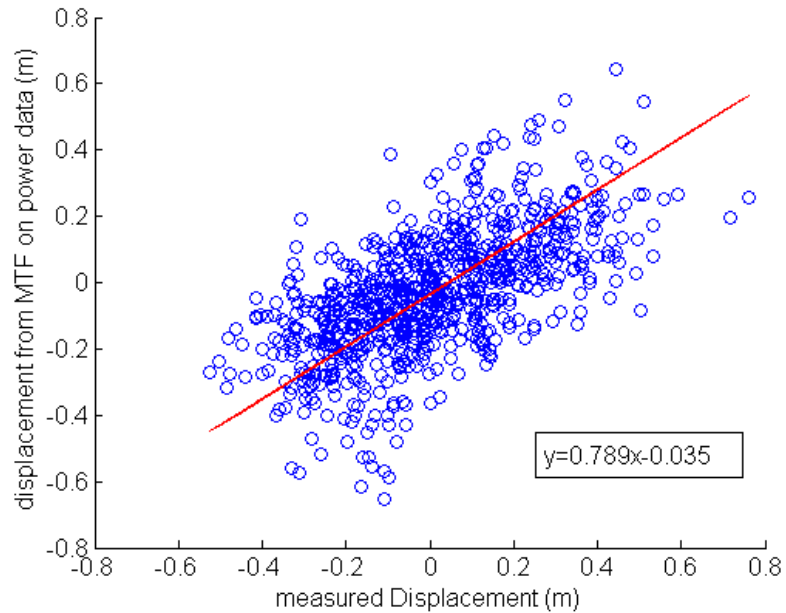


**Figure 3.20.** Scatter plot of measured displacement and displacement from parameterized MTF keeping empirical phase response at 167 m. Red line is line of best fit.

acceptable that the model does not fit the data entirely. However, it is informative to make sure that the fitted spectra are consistent with the physical environment. One of the parameters of the Pierson-Moskowitz spectrum is based on the wind speed at 19.5 m above mean sea level. The value that is chosen for this parameter to create the parameterized MTF should result in a wind speed that is physically realizable. Upon investigation, the corresponding wind speeds of the parameterized functions were generally between 10 m/s and 15 m/s. Values of wind in this range are common and not unreasonable on the ocean. Unfortunately, data about the wind speed during the deployment is unavailable at the time of writing, so no direct analysis has been done regarding the parameter values of the MTF. However, this information is thought to be on record in a data archive.

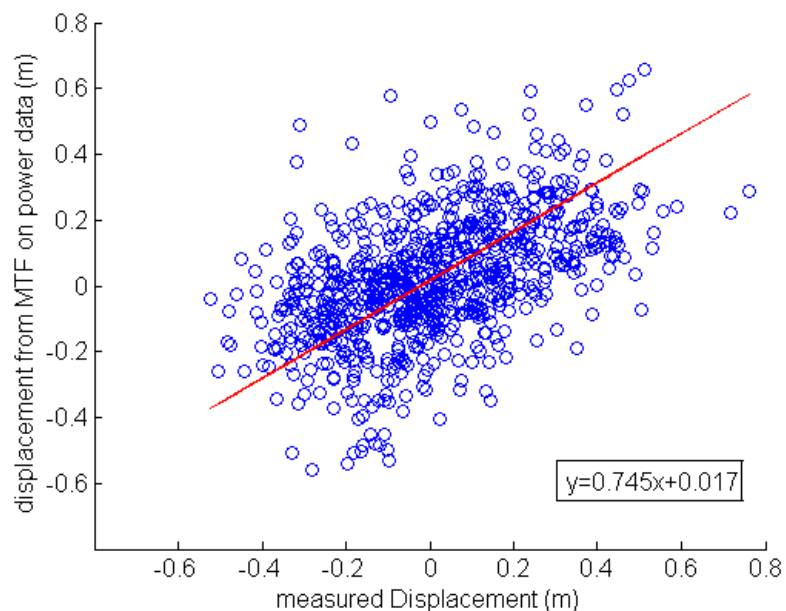


**Figure 3.21.** Scatter plot of measured displacement and displacement from parameterized MTF with constant phase response at 167 m. Red line is line of best fit.

### 3.2.6 Improved Results

Upon observing the variation in the modulation transfer functions obtained for each range and the large variation in the line of best fit for the scatter plots, it is determined that there is not enough statistical significance for any given MTF. As a result, the MTFs are averaged together to create one MTF that can be applied for any range in the image. In addition, it was determined that the dispersion filter used previously in Figure 3.9 is not filtering enough of the unwanted noise. A second filter is implemented which more closely adheres to the theoretical dispersion curve and is depicted in Figure 3.22.

The results of applying an empirical MTF with no filtering, applying the previous dispersion filter, and applying the improved dispersion filter are shown in Table 3.2. The slope of the line of best fit, the root mean square error (RMSE) between the line of best fit and the data points shown in a scatter plot of displacements, and the correlation coefficient for the data points used in a scatter plot is shown for the aver-

aged modulation transfer function applied over several range bins. It can be clearly seen from the table that there is a slight improvement in the slope and correlation using the threshold based dispersion filtering. There is a significant improvement when using the dispersion filter which is based on the theoretical dispersion curve. The correlations are close to 0.8 with a reduced RMSE and a slope closer to unity.

The empirical averaged MTF magnitude and phase along with the parameterized fits are shown in Figures 3.23 and 3.24, respectively. This transfer function which has better dispersion filtering and has been averaged over all ranges, gives improved results.

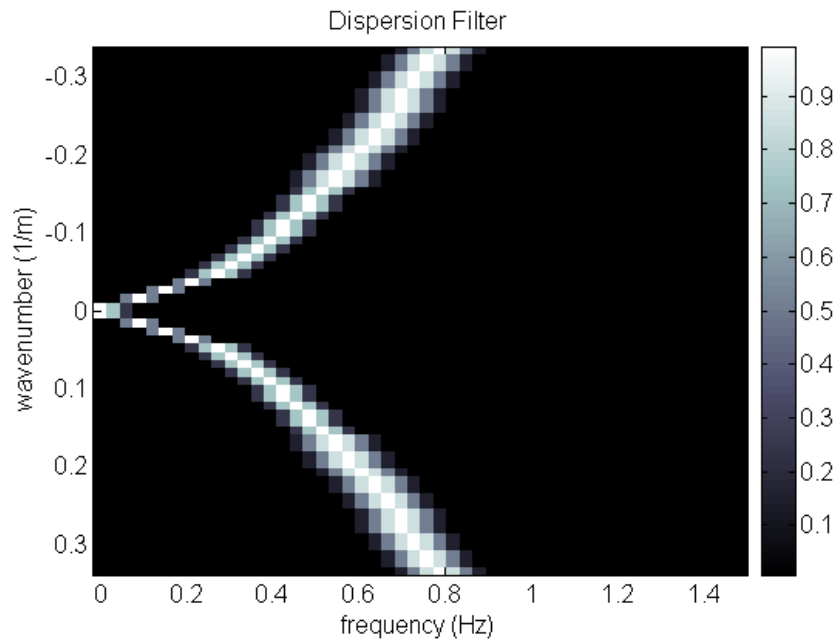


**Figure 3.22.** Improved Dispersion Filter.

The results of applying MTF shown in Figure 3.23 is shown in Table 3.3. The table shows how well the MTF is able to reproduce the measured displacements. Results are shown for the averaged empirical MTF, the parameterized MTF keeping the empirical phase response, and for the parameterized MTF with constant phase response. For each of the given MTFs, slope of the line of best fit, RMSE, and

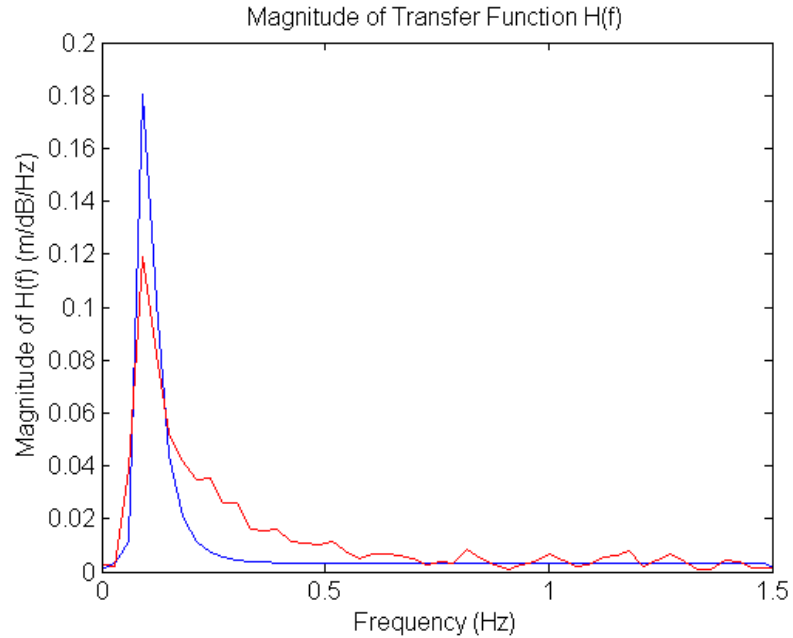


**Figure 3.23.** Averaged empirical MTF magnitude in red and parameterized MTF in blue.

correlation coefficient are given between the measured displacement and estimated displacement for several ranges. The empirical MTF without parameterization gives the best correlation and lowest RMSE of the line of best fit between the measured and estimated displacements. The high correlation and low RMSE indicates that this MTF reproduces the measured displacements well.

The parameterized versions of the MTF perform worse with lower correlations between the measured displacement and estimated displacement. The RMSE between the line of best fit is also larger for the parameterized variations. This is expected because of the fact that it is a model being fitted to the actual data and will likely have an increased error. It is expected that a unity slope would be obtained between the measured and estimated displacements, however, the empirical MTF produces a line of best fit with an average slope of approximately 0.9. Although there is not unity slope, it is a consistent value, which suggests that the MTF is a good representation.

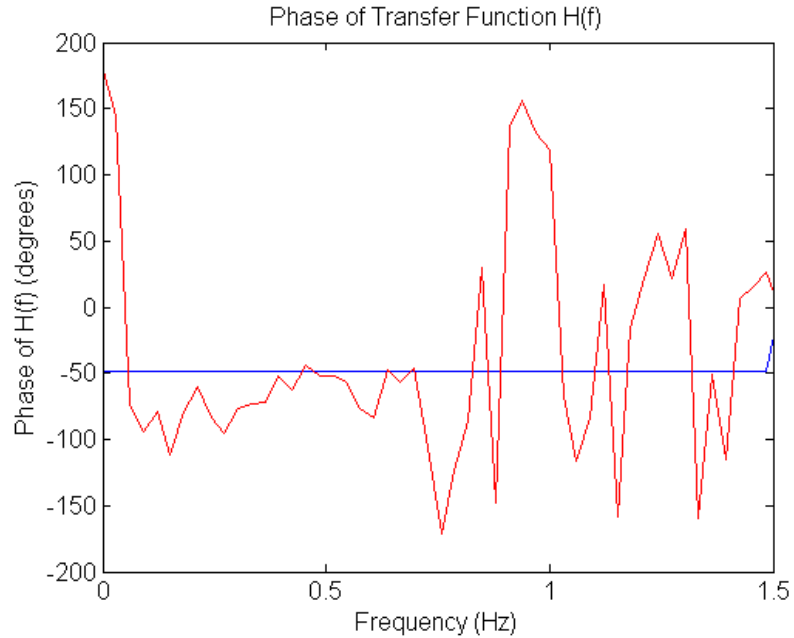


**Figure 3.24.** Averaged empirical MTF phase in red and parameterized MTF in blue.

Given the results shown in Table 3.3, by using the methods presented here, estimates of the surface displacement can be made with an accuracy of less than 10 cm when using an empirical MTF without parameterization. A small gain will likely have to be applied when using the empirical MTF in order to bring the slope of the line of best fit from approximately 0.9 to unity. When using a parameterized MTF, an accuracy of 15 cm or less can be achieved when applying to filtered power data.

Range (m)	Empirical MTF with no dispersion filter			Empirical MTF filtered according to Figure 3.9			Empirical MTF filtered according to Figure 3.22		
	Slope	RMSE (m)	Correlation	Slope	RMSE (m)	Correlation	Slope	RMSE (m)	Correlation
150	0.41	0.11	0.63	0.62	0.12	0.58	1.00	0.06	0.82
151.5	0.40	0.12	0.53	0.41	0.10	0.65	0.95	0.06	0.82
153	0.51	0.12	0.53	0.50	0.10	0.66	0.93	0.06	0.80
165	0.45	0.10	0.65	0.51	0.09	0.72	0.91	0.07	0.71
166.5	0.42	0.12	0.52	0.50	0.11	0.64	0.92	0.07	0.72
168	0.37	0.11	0.52	0.52	0.10	0.67	0.93	0.07	0.73
172.5	0.41	0.12	0.54	0.50	0.11	0.63	0.94	0.07	0.79
174	0.43	0.13	0.48	0.48	0.12	0.57	0.93	0.07	0.81
175.5	0.45	0.13	0.50	0.47	0.11	0.58	0.93	0.06	0.82
193.5	0.47	0.13	0.54	0.58	0.12	0.64	0.89	0.07	0.77
195	0.49	0.11	0.65	0.58	0.11	0.69	0.90	0.07	0.76
198	0.47	0.12	0.58	0.56	0.11	0.67	0.88	0.08	0.76
213	0.60	0.16	0.55	0.73	0.15	0.63	1.00	0.06	0.86
214.5	0.52	0.15	0.50	0.64	0.14	0.62	0.98	0.06	0.85
216	0.37	0.14	0.44	0.57	0.13	0.58	0.97	0.06	0.84

**Table 3.2.** Error in empirical MTFs when varying dispersion filter.

Range (m)	Empirical MTF			Parameterized MTF with empirical phase			Parameterized MTF with constant phase		
	Slope	RMSE (m)	Correlation	Slope	RMSE (m)	Correlation	Slope	RMSE (m)	Correlation
150	1.00	0.06	0.82	1.39	0.10	0.73	1.49	0.12	0.59
151.5	0.95	0.06	0.82	1.32	0.10	0.70	1.39	0.12	0.58
153	0.93	0.06	0.80	1.28	0.10	0.68	1.33	0.12	0.58
165	0.91	0.07	0.71	1.30	0.12	0.56	1.40	0.15	0.43
166.5	0.92	0.07	0.72	1.33	0.12	0.57	1.47	0.15	0.42
168	0.93	0.07	0.73	1.36	0.12	0.59	1.53	0.15	0.42
172.5	0.94	0.07	0.79	1.30	0.11	0.66	1.43	0.15	0.48
174	0.93	0.07	0.81	1.26	0.11	0.68	1.36	0.14	0.51
175.5	0.93	0.06	0.82	1.24	0.10	0.71	1.32	0.13	0.54
193.5	0.89	0.07	0.77	1.17	0.11	0.66	1.20	0.13	0.57
195	0.90	0.07	0.76	1.16	0.11	0.65	1.20	0.13	0.55
198	0.88	0.08	0.76	1.16	0.12	0.65	1.20	0.14	0.52
213	1.00	0.06	0.86	1.28	0.10	0.78	1.33	0.12	0.65
214.5	0.98	0.06	0.85	1.26	0.10	0.77	1.30	0.12	0.66
216	0.97	0.06	0.84	1.25	0.10	0.77	1.29	0.12	0.67

**Table 3.3.** Error in MTFs using improved dispersion filtering and averaged MTF as base for parameterizations.

### 3.2.7 Comparison with Phillips Spectrum

The Phillips spectrum is another model for ocean waves and is defined by equation (2.7). This model, created in the 1950s, characterized ocean wave spectra in the region where the spectrum decayed at higher frequencies. In the same manner to the Pierson-Moskowitz spectrum, this model is fit in a least squares sense to the data to create a MTF. The resulting MTF is then applied to the second half of the data and evaluated. A scatter plot shown in Figure 3.25 is obtained when plotting measured displacement against the displacement from the Phillips MTF. It is evident from the scatter plot that the results from the MTF are not valid. The problem is that the Phillips spectrum approaches infinity as the frequency approaches zero. Since the actual spectrum does not behave in this manner, the results are invalid. The large low frequency components dominate the displacements created by the MTF.

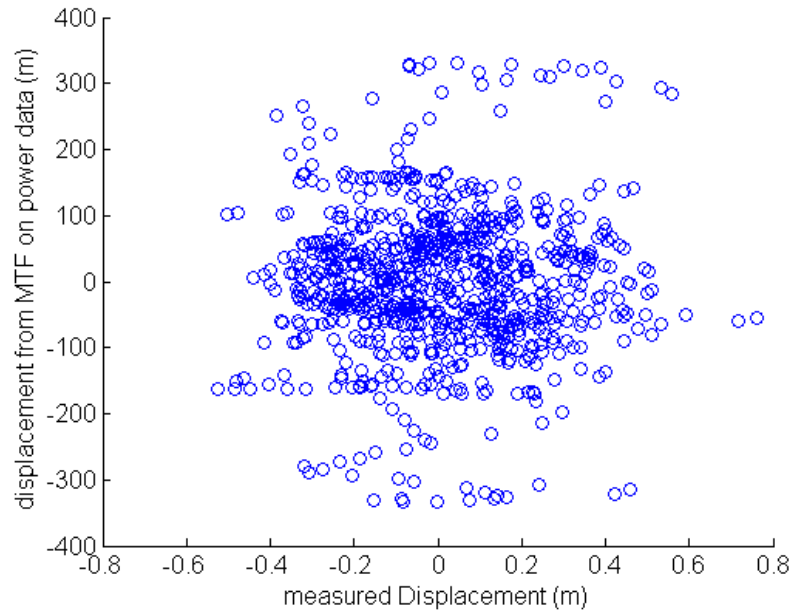


**Figure 3.25.** Scatter plot of measured displacement and displacement from Phillips spectrum keeping phase response of empirical MTF at 167 m.

## CHAPTER 4

### DUAL POLARIZATION ANALYSIS

#### 4.1 Hilbert Transform on Displacement and Wave Envelope

An area of interest in the study of radar measurements of the ocean surface are the impulsive and strong echoes received using horizontal polarization. This is of particular interest in detecting small boats or other objects since these strong echoes which are often associated with waves that are breaking, may obscure such targets. The predominant scattering mechanism is non-Bragg and remains poorly understood. Figure 4.1 shows an example of data collected from the FOPAIR radar with horizontal polarization. There is less contrast of the ocean waves in this image and frequent bright returns. It is desirable to determine a correlation between these bright returns in the H-Pol data and the characteristic of the displacement imagery. For example, it is thought that a steep slope on the advancing ocean waves will produce a strong H-Pol return.

The sea spikes are present in both the power data and velocity data and are thought to be associated with certain characteristics of the wave envelope. It is thought that when the wave envelope becomes large, likely resulting in a steep slope near the crest, there is a greater chance of encountering sea spikes. In addition, the sea spikes tend to be associated with the front of advancing waves near the top, which is where there is a steep slope and whitecapping can occur. This section describes how the 1996 data set is processed in order to associate sea spikes to a location of the wave envelope.

It will be shown in this chapter that H-Pol sea spikes occur most frequently on the front face of the wave group envelope and for medium to large envelope amplitudes. It will also be shown that these sea spikes are also present in the V-Pol imagery.

To evaluate where on the ocean wave profile the spikes in power originate, a 2-D Hilbert transform can be taken of displacement images. Using the original image and its Hilbert transform, one can construct an image of amplitude and phase. This analytic signal describes the complex envelope,  $A(t)e^{j\phi(t)}$ , whose real part is the observed displacement. The angle  $\phi(t)$  indicates the instantaneous phase of a pixel with respect to a reference cosine. The phase of the transform with relation to the displacement profile is depicted in Figure 4.2. Assuming a sinusoid as the wave envelope, the phase of the envelope will be the same as given in the figure. Because sea spikes can be

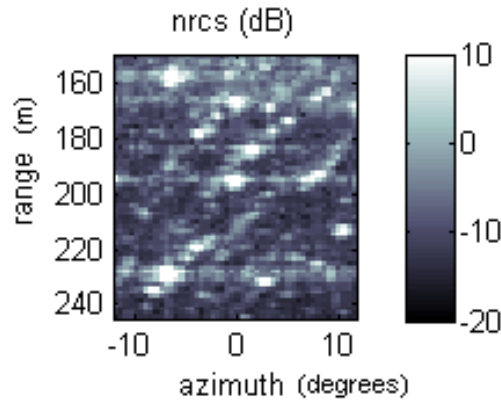


**Figure 4.1.** Horizontal polarization NRCS imagery.

associated with large waves (as previously discribed), H-Pol spikes occur more frequently when the wave amplitude,  $A$ , is large. The complex envelope can be useful in that the magnitude describes the wave group envelope.

A few plots can be produced by using the complex envelope. One type of plot can show averaged backscattered power or Doppler velocity vs the phase of the wave envelope. To produce a plot like this on V-Pol power, the 33 second power image similar to that shown in Figure 3.3 and the equivalent displacement image are passed

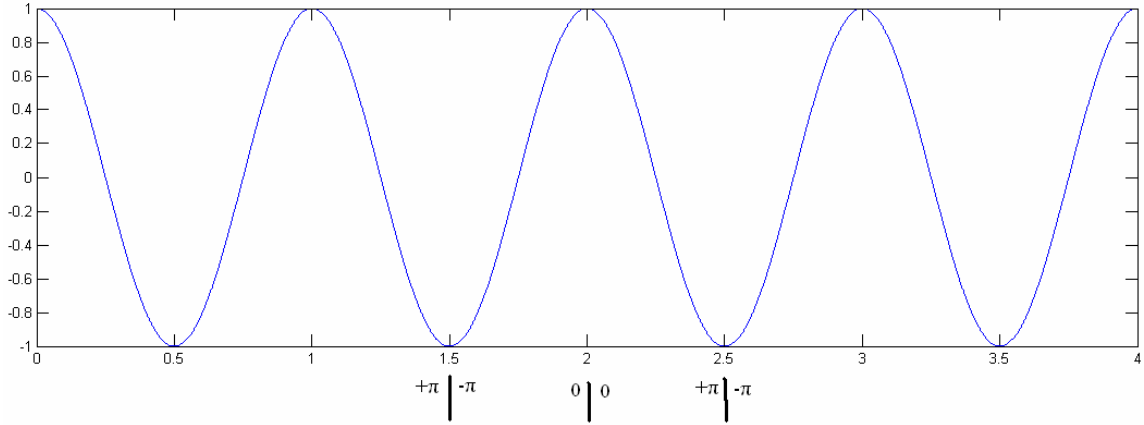


**Figure 4.2.** Phase of wave envelope for segments of a sinusoidal wave envelope profile.

through a dispersion relation filter. When performing analysis of H-Pol data, the dispersion relation filter is only applied to the displacement imagery. There are now two filtered range verses time images, one of power and one of displacement. The displacement image is passed through a Hilbert transform and combined with the original image yielding complex numbers for each pixel which represent the complex envelope. A loop cycles through increments of phase. For a given phase of a pixel in the complex envelope image, the corresponding pixel from the power image is taken and summed with other pixels of the same phase. The summation is divided by the number of pixels used to generate sum and this process is averaged over separate 33 segment images in order to create a plot of averaged backscattered power for a given phase of the ocean wave group envelope.

Another way of illustrating the method for creating the plot is shown in Figure 4.3. The image shows three circles, in the left most array, that correspond to complex numbers from the complex envelope. These circles all have about the same phase. The same pixels are selected from the corresponding power image array as represented by the squares in the middle array. Those three values from the middle array are then summed together and mapped to the array on the right, as shown by the diamond.

This sums all of the power elements whose wave group envelopes have the same phase. This technique can also be applied to the velocity data to obtain a plot of averaged velocity at a given phase or applied to the displacement imagery to get a plot of the average wave envelope profile. By applying the procedure to power imagery, plots can be generated which give an indication as to where most of the backscattered power originates from the wave group envelope. Additionally, instead of sorting based on the phase envelope, sorting can be based on the magnitude. This will give information on what magnitudes of the complex wave envelope yield the most backscattered power.

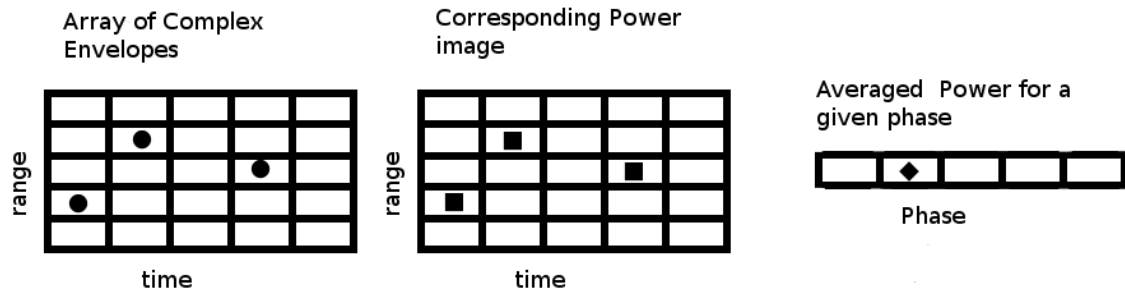


**Figure 4.3.** Process for creating image of power distribution with respect to complex wave envelope characteristics 1-D.

Although plots of average power for a given instantaneous phase are useful, they do not provide a full picture. In this case, there is no information about what magnitudes of the complex wave envelope went into each phase bin to create the plot. A more revealing image would show the phase envelope on one axis and the magnitude of the envelope on the other axis. The intensity of each pixel in this image could be the average power that is associated with having the given magnitude and phase of the complex envelope. To create the type of plot described, it is necessary to cycle through both phase, as done previously, and through magnitude. A two dimensional array where one dimension is phase and the other is magnitude accumulates the pixels from

the power imagery whose corresponding displacement pixel has the given complex envelope magnitude and phase. First a list of pixels that are within a given complex envelope phase interval is extracted and those pixels are then sorted according to the magnitude of the complex envelope. This process results in adding values to the two dimensional array one column at a time until it is full. Each value in the summation array is divided by the total pixels put into that position and averaged over sequential images.

Once again, an image describing the process can be useful in understanding the process. Figure 4.4 shows the three arrays involved in obtaining the final image. The array on the left is the complex envelope which has three circles representing values in the array with nearly the same magnitude and phase. The same pixels from the corresponding power image are selected and summed together. The sum is added to the appropriate location, as shown by the diamond, for the designated magnitude and phase that the points share in the right most array. This maps the power values which come from a common wave profile into one point in the right array. The procedure described can be applied to the velocity imagery as well in order to determine where the highest velocities originate from on the wave group envelope.

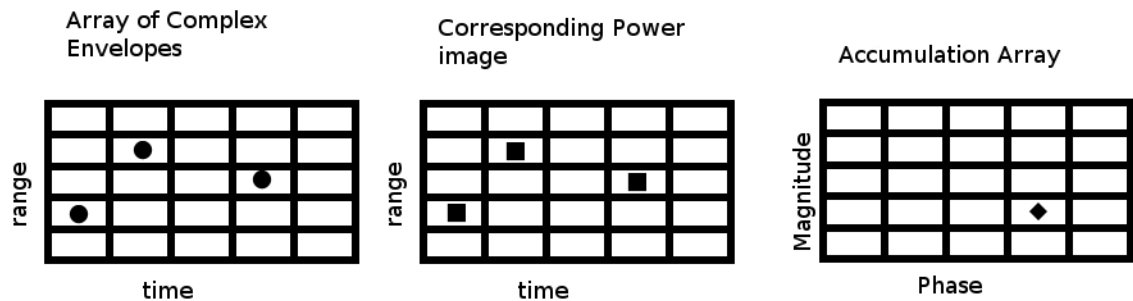


**Figure 4.4.** Process for creating image of power distribution with respect to complex wave envelope characteristics 2-D.

The described plots for associating average power levels or velocity with a characteristic of the complex wave envelope employs no thresholding other than the dispersion relation used to filter the displacement. However, an area of interest for this thesis is associating bright sea spikes to a characteristic of the complex wave envelope. Because the sea spikes are usually much brighter than the rest of the image, thresholding of the plots based on the power is performed. To accomplish the necessary thresholding, empirically computed cumulative distribution functions of both the V-Pol and H-Pol power are created. A value of power is selected in which 90% of the power is less than that value. Thresholding is performed in creating the complex envelope plots where only the upper 10% is included in order to essentially only count sea spikes.

## 4.2 Sea Spike Analysis

It is informative to perform the previously described analysis on the wave displacement in order to get a plot of the average wave envelope profile as shown in Figure 4.5. As expected, the envelope is generally of a shape similar to a sinusoid, although it is actually slightly more pointed at the peak. Figure 4.5 provides a means of associating locations on similar plots based on power or velocity to a location on the complex wave envelope.

A similar plot to Figure 4.5 can be created based on the V-Pol and H-Pol backscattered power. Figures 4.6 and 4.7 display the average V-Pol and H-Pol backscattered power as a function of the phase of the complex wave envelope, respectively. It can be noted that the V-Pol plot better represents a sinusoid than the H-Pol plot. The relatively sinusoidal nature of the V-Pol power plot is expected because the backscattered mechanism is predominantly Bragg scattering with tilt modulation and hydrodynamic effects which modulate the power. In contrast, the H-Pol backscattered power is primarily based on non-Bragg scattering and has large sea spike returns that

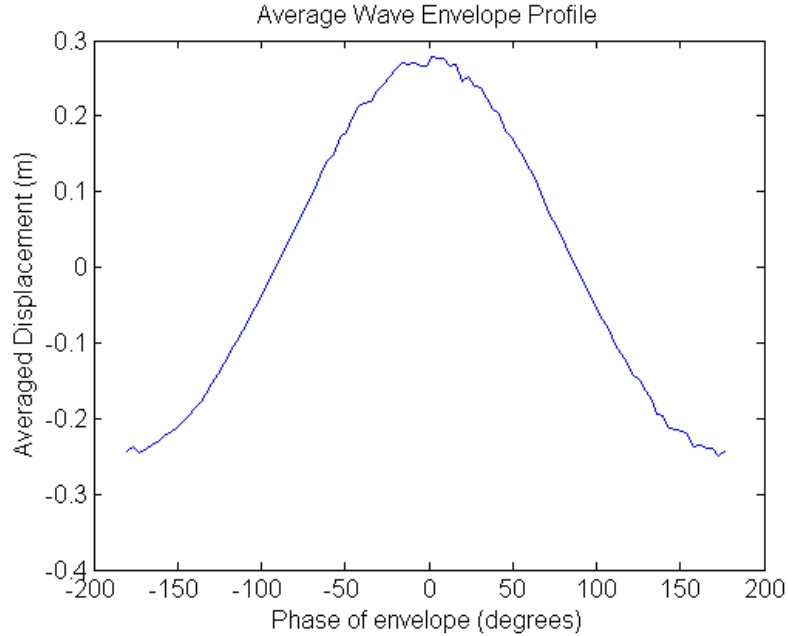


**Figure 4.5.** Average wave envelope profile as a function of the phase of the complex envelope.

can dominate. As expected, when comparing Figure 4.6 and 4.5, most of the V-Pol backscattered power originates from the front face of the displacement profile, corresponding to phases between  $0^\circ$  and  $-180^\circ$ . There is significantly less V-Pol power from the back face of the wave due to tilt modulation and possibly shadowing. In the H-Pol plot of Figure 4.7, the majority of the backscattered power originates from the front face toward the top of the wave profile for phases between  $-90^\circ$  and approximately  $0^\circ$ . This agrees well with theories that sea spikes are associated whitecapping and steep wave features that would be encountered on the front face near the peak of the wave. These events provide a large return at a given location on the wave but very little power for other locations on the profile, which is evident in the H-Pol Figure.

In addition to viewing the power distribution with respect to the average envelope profile, plots of velocity are created. The same procedure as described for the previous plots is employed but the pixels from a given phase of the complex envelope are

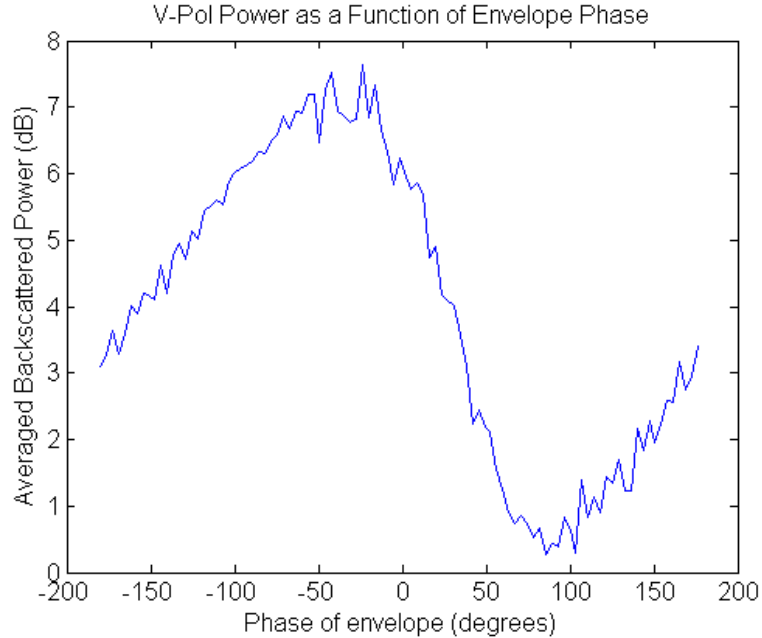


**Figure 4.6.** Average V-Pol backscattered power as a function of the phase of the complex wave envelope.

associated with the equivalent pixels in the velocity data. Figures 4.8 and 4.9 show the average V-Pol and H-Pol velocity against the phase of the complex wave envelope, respectively. In the V-Pol plot the mean velocity is removed prior to the creation of the plot. As expected in V-Pol velocity measurements, the maximum velocity corresponds to the peak of the average wave envelope. The peak of a wave is where the orbital velocity is maximum and at the trough the orbital velocity is minimum. In the H-Pol plot, only pixels where the corresponding power pixel was in the top 10% are included in the analysis. Only pixels that correspond to large power are included because the sea spikes in the velocity imagery have range sidelobes that are less prevalent in the power imagery. In order to determine where the sea spikes in velocity data originate, it is necessary to filter according to the power data. Figure 4.9 shows the largest velocities centered about the peak of the wave envelope profile. The centered H-Pol velocity profile suggests that the Doppler velocity is maximum at the peak of the wave envelope where as the H-Pol power is maximum slightly before the

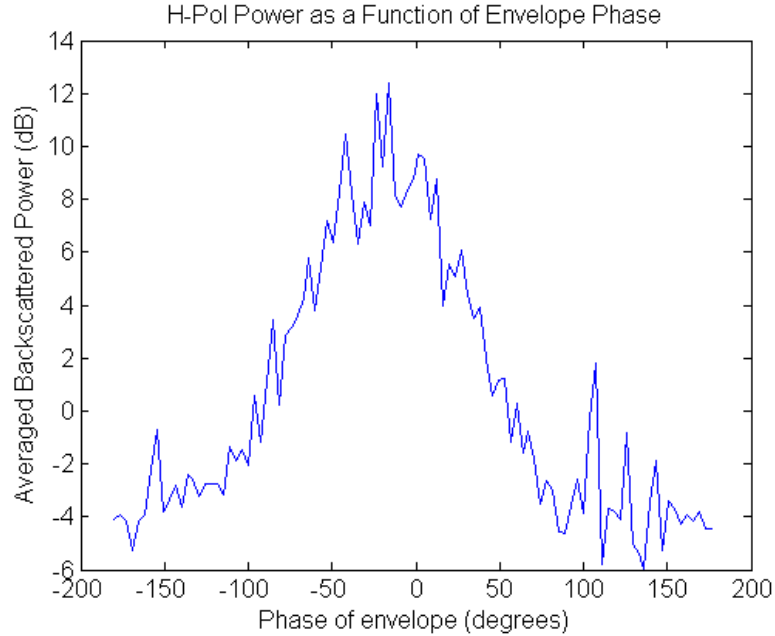


**Figure 4.7.** Average H-Pol backscattered power as a function of the phase of the complex wave envelope.

peak. Although this method provides information about where the largest velocities or the majority of the power originate, it does not separate out the size of the complex wave envelopes that go into each phase bin in the plots.

A more revealing way of observing the origin of H-Pol spikes is to create an image where the magnitude of the complex wave envelope is on one axis, the phase is on the other axis, and the pixel intensity corresponds to the average value of power or velocity that is observed. The magnitude axis describes the height of the wave envelope. By sorting the complex wave envelope magnitude, one can better observe what magnitude and location on the wave envelope present greater returns. The images are generated using pixels corresponding to the upper 10% of the backscattered power. By limiting to the largest power echos, the plots primarily show where the sea spike power is located with respect to the envelope characteristics. A fairly coarse bin size is selected for the images in order to ensure that enough data points are mapped

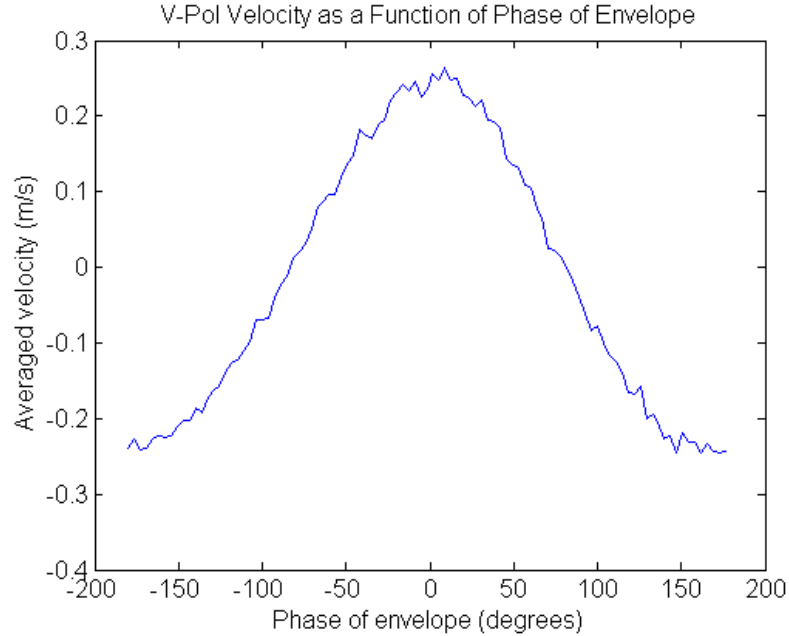


**Figure 4.8.** Average V-Pol velocity as a function of the phase of the complex wave envelope.

to a given bin. With a finer resolution, areas of the image have one pixel having a large value and the adjacent pixel having no value.

Figures 4.10 and 4.11 display the average V-Pol and H-Pol backscattered power originating from a given portion of the complex wave envelope, respectively. In the V-Pol image of Figure 4.10, a greater amount of backscattered power occurs for phases corresponding to the front face of the wave envelope. Furthermore, for a horizontal line at a large wave amplitude, for example at 0.9 m, nearly all the backscattered power is associated with the top half of the front face of the wave envelope. At large envelope amplitudes, there is severe tilt modulation and likely shadowing of areas behind the large peak. For envelope magnitudes less than about 0.5 m, there is a fairly continuous modulation of power indicating standard tilt modulation and no shadowing. In the H-Pol Figure, a similar trend exists however there is a very pronounced region of large backscattered power. For amplitudes exceeding 0.5 m and phases corresponding to the front face of the wave, there is an area of large H-Pol

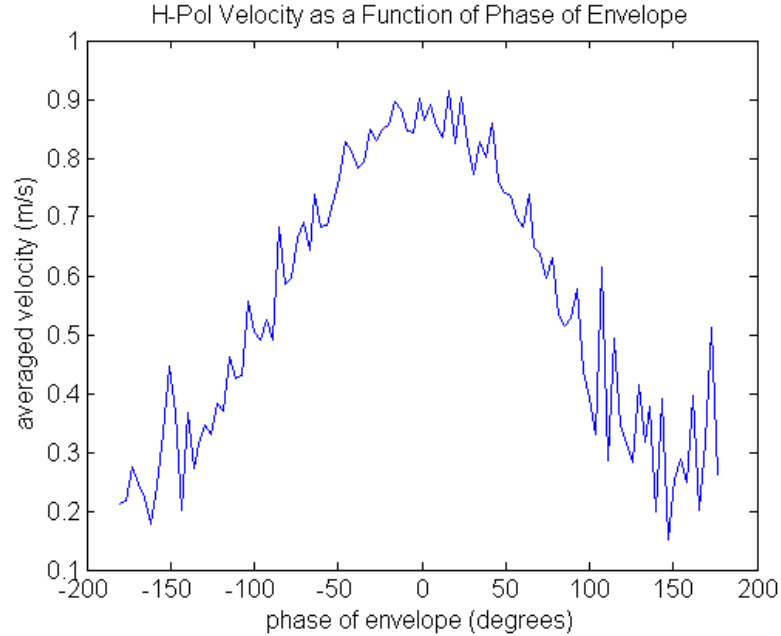


**Figure 4.9.** Average H-Pol velocity of the corresponding to the top 10 percent of power as a function of the phase of the complex wave envelope.

backscattered power. It is this region in the H-pol power image that corresponds to the sea spikes visible in the H-Pol power data. Plots of the number of data points from the power imagery that is used to create one pixel in figures 4.10 and 4.11 are present in Appendix B. The results presented in the two discussed figures confirm current theories that sea spikes in the H-Pol power imagery are associated with echoes from the front face of larger amplitude waves that are becoming steep.

In addition to observing sea spikes in H-Pol power imagery, they are also present in the Doppler velocity imagery. Again, plots of where the highest velocities occur with respect to envelope characteristics is created in the same manner as the images for backscattered power and filtered according to the top 10% of power. Figures 4.12 and 4.13 display the allocation of measured velocities with respect to the complex wave envelope magnitude and phase. For complex wave envelope magnitudes greater than about 0.6 m in the V-Pol velocity image the measured velocities are consistently positive. Not only are the velocities predominantly positive in this region, but the

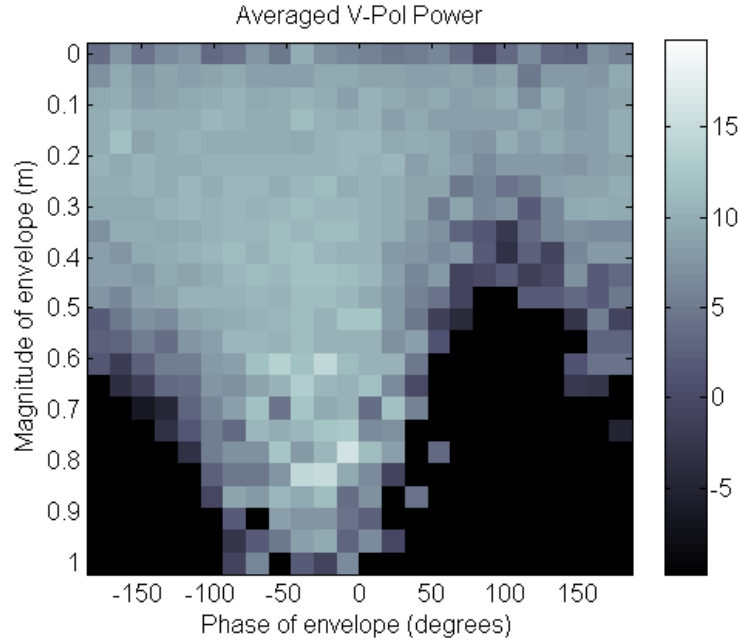


**Figure 4.10.** Average V-Pol power, in dB, mapped to complex wave envelope magnitude and phase.

largest velocities are located on the front face of the wave envelope profile. In much the same way that the power is predominantly from the front faces of large amplitude envelopes, the velocity in V-Pol is maximum in the same region. Because little negative velocity is seen for large wave envelopes, there is likely shadowing occurring that prevents the measurement of the orbital velocities in the troughs of large waves. It is interesting to observe that the areas of highest velocities are not concentrated at the largest complex wave envelope magnitudes. The majority of larger velocity measurements occur for envelope magnitudes between 0.4 m to 0.9 m. One would expect the measured velocities to increase with increased amplitude of the complex wave envelope, which does occur to a degree. For envelopes less than 0.4 m, there is a continuous increase of velocity as amplitude increases. However, for envelopes greater than 0.4 m there is little change in maximum velocity before declining at larger amplitudes. The decline at the largest amplitudes may be due to few waves measured which have an envelope that large.

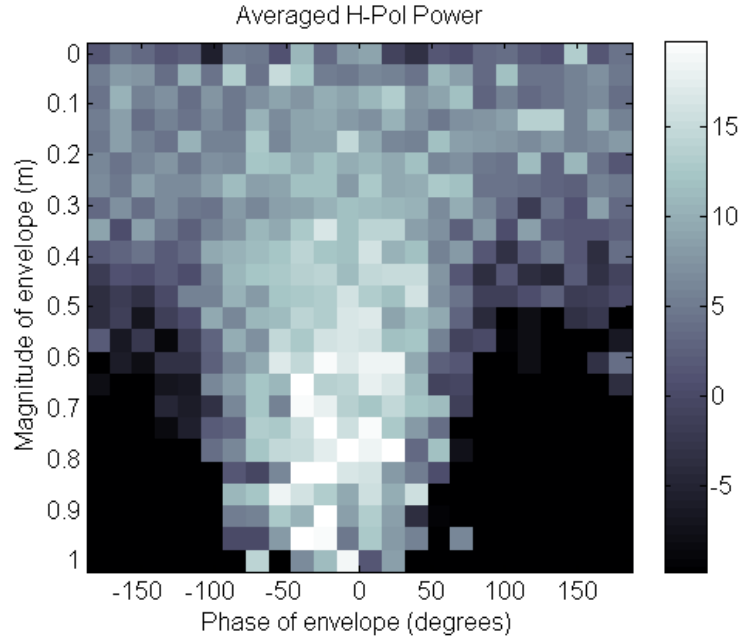


**Figure 4.11.** Average H-Pol power, in dB, mapped to complex wave envelope magnitude and phase.

Figure 4.13 shows the H-Pol velocities measured and generally has larger values than the V-Pol image. Since the images are created using data points which mostly contain sea spikes, it is expected for there to be large velocities shown in the H-Pol image. Again, the area of highest velocities is slightly toward negative phases for peak H-Pol velocities occurring on the front face of the wave envelope. The Doppler velocities are maximum for amplitudes between 0.4 m and 0.8 m, a somewhat unexpected result. It is believed that H-Pol sea spikes were associated with larger waves, however the results show that the H-Pol velocity sea spikes are not highly dependent on the size of the wave envelope. It appears that the velocities associated with H-Pol sea spikes are not as heavily correlated with envelope magnitude as compared to the backscattered power. This is an interesting result that should be confirmed with more data sets to be sure it is not an artifact of the test conditions or of the radar system.

An additional point of interest arises in looking at the location of highest velocities between the H-Pol and V-Pol images. The area of highest velocities is associated with

approximately the same envelope characteristics in the V-Pol and H-Pol images. The occurrence of H-Pol sea spikes which also present spikes in the V-Pol data agrees with current theories that a sea spike event in H-Pol is also present in the V-Pol data. However, due to Bragg scattering, the sea spike event in V-Pol is essentially obscured. By limiting to large backscatter power values, it is possible to see the effects of sea spikes in the V-pol imagery more clearly.

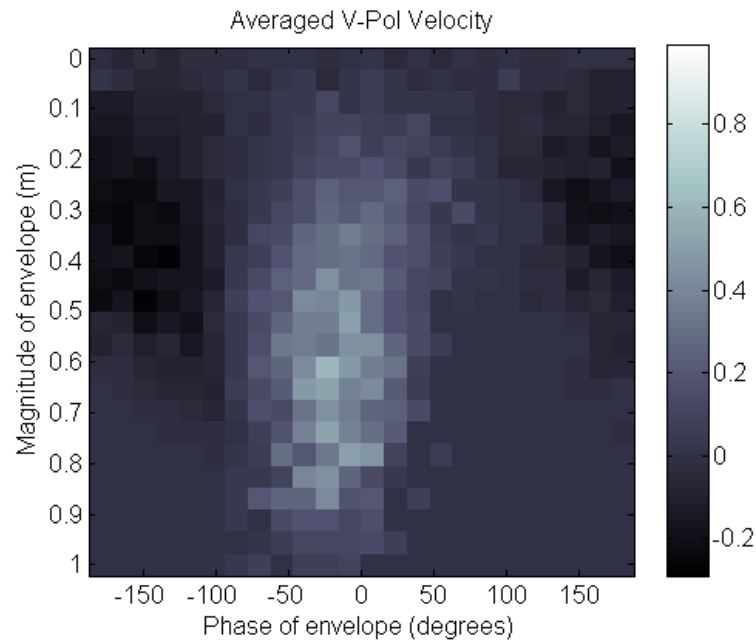


**Figure 4.12.** Average V-Pol velocity, in m/s, mapped to complex wave envelope magnitude and phase.

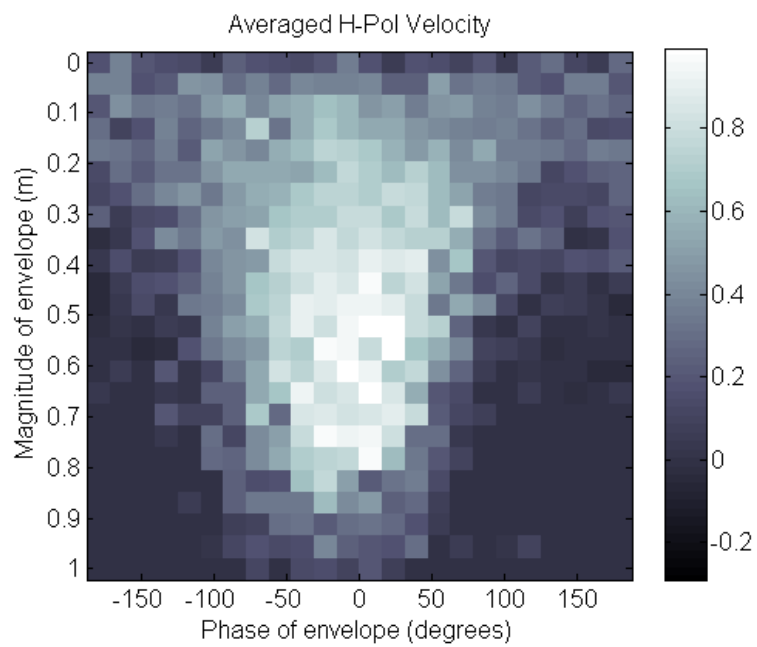


**Figure 4.13.** Average H-Pol velocity, in m/s, mapped to complex wave envelope magnitude and phase.

## CHAPTER 5

### CONCLUSIONS

#### 5.1 Application of a MTF

Using radar backscattered power data of the ocean surface to approximate the surface topography is an area of interest for Oceanography, the shipping industry, and the navy. In this thesis, a method for developing a modulation transfer function (MTF) has been discussed. This MTF attempts to invert several radar scattering and imaging mechanisms that modulate the backscattered signal in order to reconstruct the surface displacement at a location over a time sequence solely from the power data. To ensure validity of the data, spectra of the displacement and power are compared with theory. Filtering about the dispersion relation for gravity waves is performed to reduce noise in the signal.

Histograms and scatter plots show the effectiveness of both parameterized and non-parameterized MTFs for a range of 167 m. The non-parameterized MTF reproduced the displacement profile well with a near one to one correspondence between measured displacements and results from the MTF. The parameterized MTF does not give as good of results with a scatter plot line of best fit with a slope further from unity and a histogram closer to a normal distribution than the measured displacement distribution. This increase in error from the parameterized MTF is likely due to variations of the true MTF that deviate from the parameterized model where the spectrum is coherent.

An improvement on the dispersion relation filtering and averaging the modulation transfer functions for all the range bins increased the accuracy of this inversion

technique. With this improvement, estimates of displacement using a MTF can be accurate to less than 10 cm.

## 5.2 Sea Spike Locations

Sea spikes are most noticeable in H-Pol imagery of the ocean surface. Sea spikes are of interest to marine radar engineers as well as the navy in order to distinguish sea clutter from other objects on the ocean. Some people in the area of marine radar imaging have noticed a correlation between sea spikes and waves that are either white-capping or near breaking. This thesis associated sea spikes with the wave envelope height and location on the wave envelope profile. This association is built on pixels which present the most backscattered power, likely corresponding to sea spikes. Plots generally agree with current theories of wave features that are correlated with sea spikes. A large amount of backscattered power is present on the front face of the wave and is primarily present for larger wave envelopes. The peak velocities also follow this trend but have much less dependence on the magnitude of the complex wave envelope. This suggests that in terms of the Doppler velocity, the sea spikes are not highly dependent on whether the complex wave envelope is large or small. In addition, the V-Pol images showed maximum returns for similar complex wave envelope characteristics as the H-Pol . This suggests that the sea spikes that are present in H-Pol imagery are also present in V-Pol but are less noticeable due to Bragg scattering in V-Pol.

## 5.3 Areas of Future Work

The development and analysis performed in this thesis for the development of a MTF is based on data where the surface topography was neither measured remotely nor *in situ*. As a result, the MTF is based on velocity data that has been transformed to displacement in order to obtain a topographic image. This is generally accepted

by marine radar engineers, but it is not a direct measurement of the displacement. It is possible that there is error in the computed displacement which can not be rectified. The data set collected in 2000 measured the surface using interferometry, however the validity of the displacements could not be verified against theory. Future work could focus on data sets from a radar where the interferometric displacement agrees with ocean wave theory and where there is data from *in situ* devices. By measuring the interferometric and *in situ* displacement, the confidence can be greater for establishing a link between power and displacement data. In addition, data sets from varying conditions should be analyzed to determine how the relationship varies for different conditions. For example, the results from using a parameterized MTF may be better if conditions more closely match a fully developed sea.

The analysis on sea spikes is performed using the same data set used to generate the MTF and could also benefit from having true interferometric data for displacement. The complex wave envelope analysis is based on the displacement data, which is created using the velocity data in this thesis. Having a more direct measurement of the surface displacement would be beneficial in fully establishing the results. In addition, several data sets should be analyzed to confirm the characteristics of sea spikes for different sea states.

## APPENDIX A

### SAMPLE MODULATION TRANSFER FUNCTIONS FOR DIFFERENT RANGES

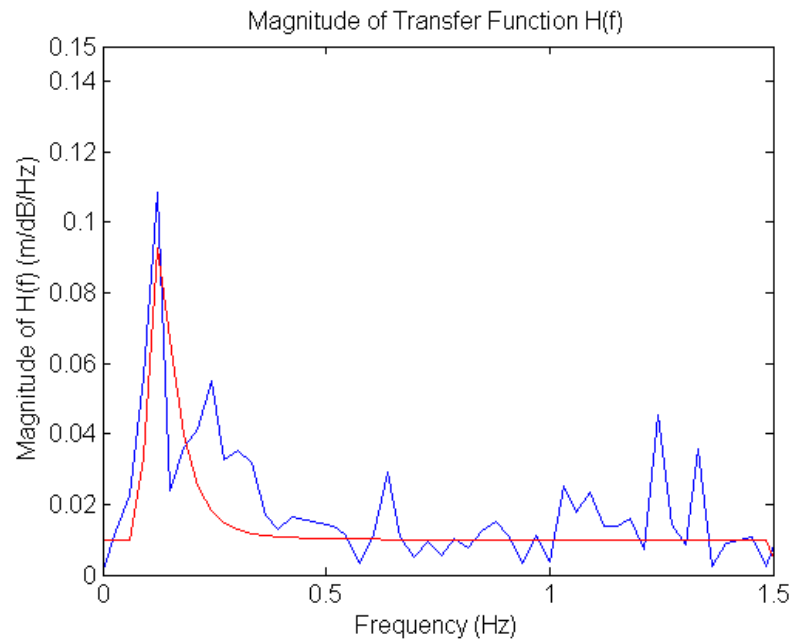


**Figure A.1.** Magnitude of Transfer function for range of 152 m.

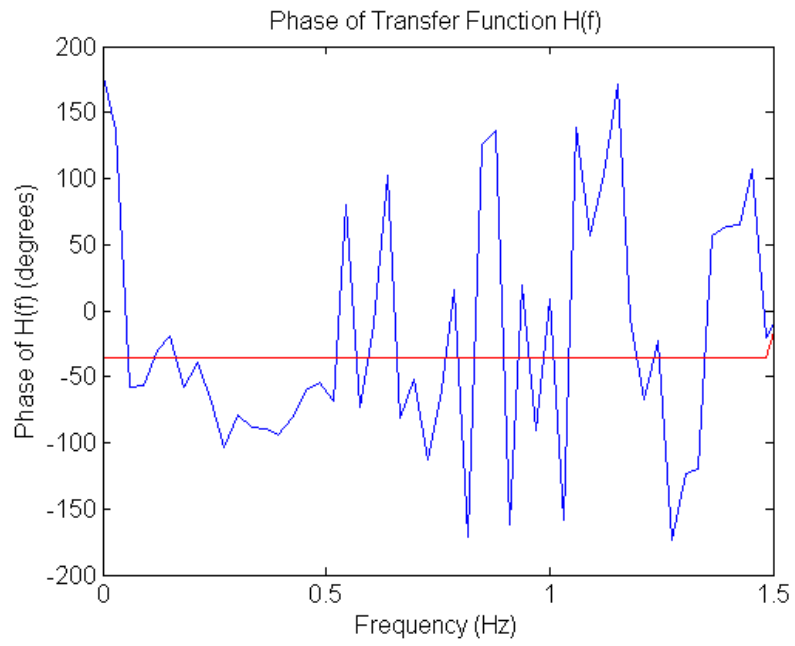


**Figure A.2.** Angle of Transfer function for range of 152 m.

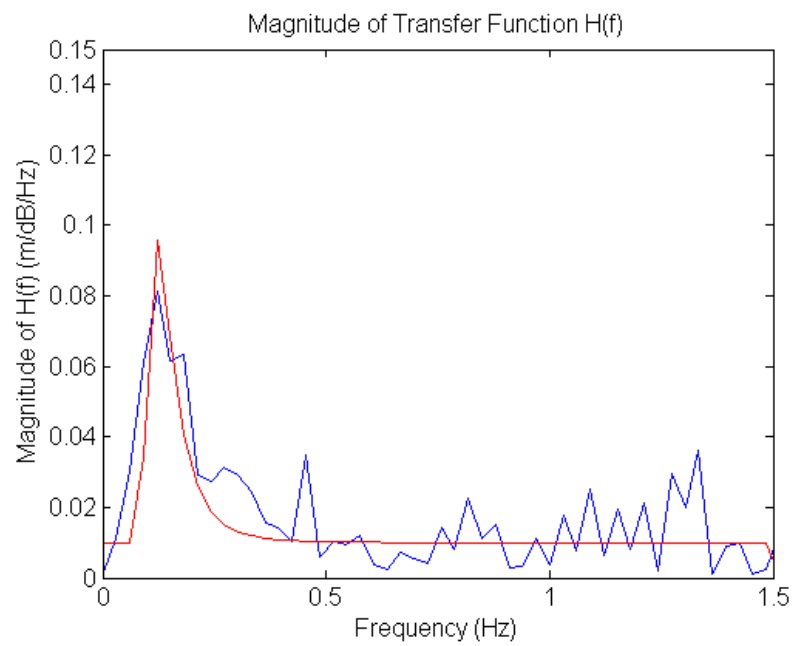


**Figure A.3.** Magnitude of Transfer function for range of 174 m.

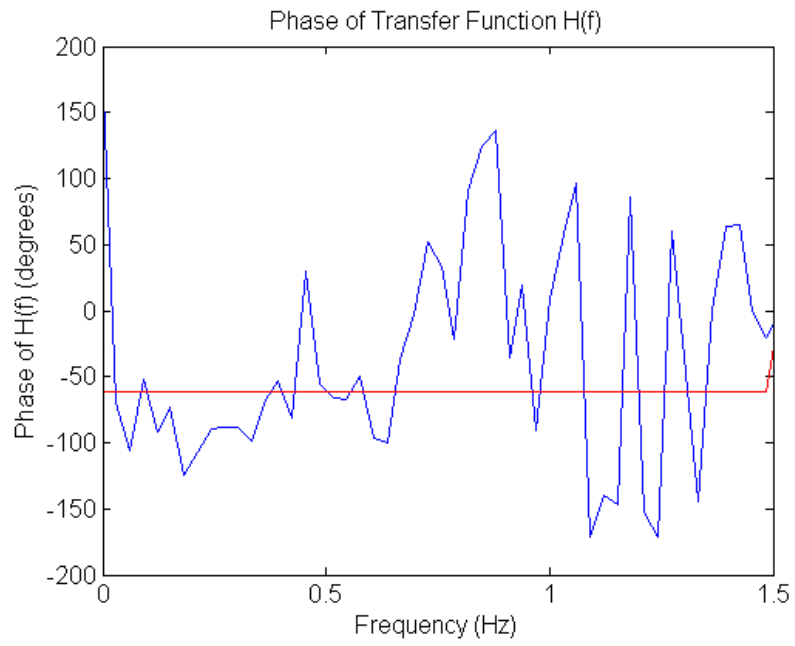


**Figure A.4.** Angle of Transfer function for range of 174 m.

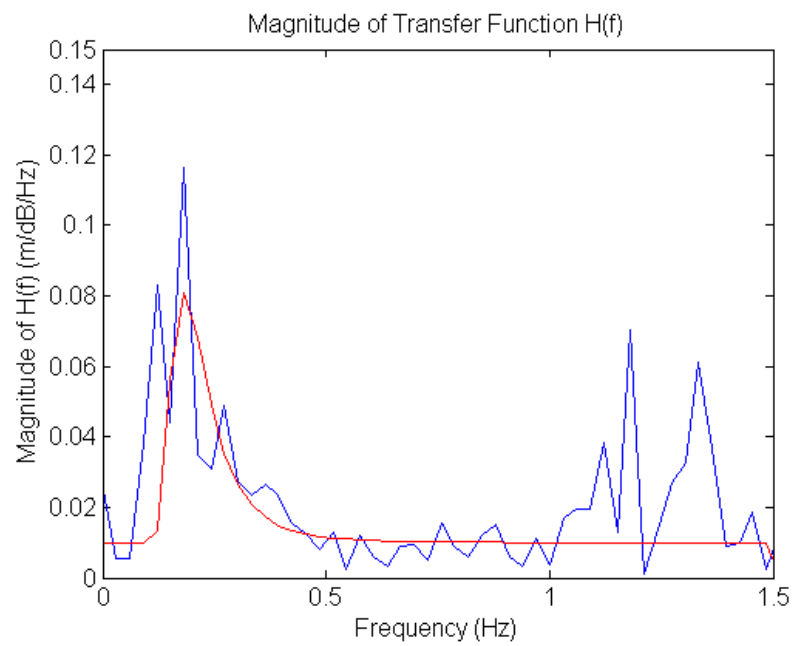


**Figure A.5.** Magnitude of Transfer function for range of 195 m.

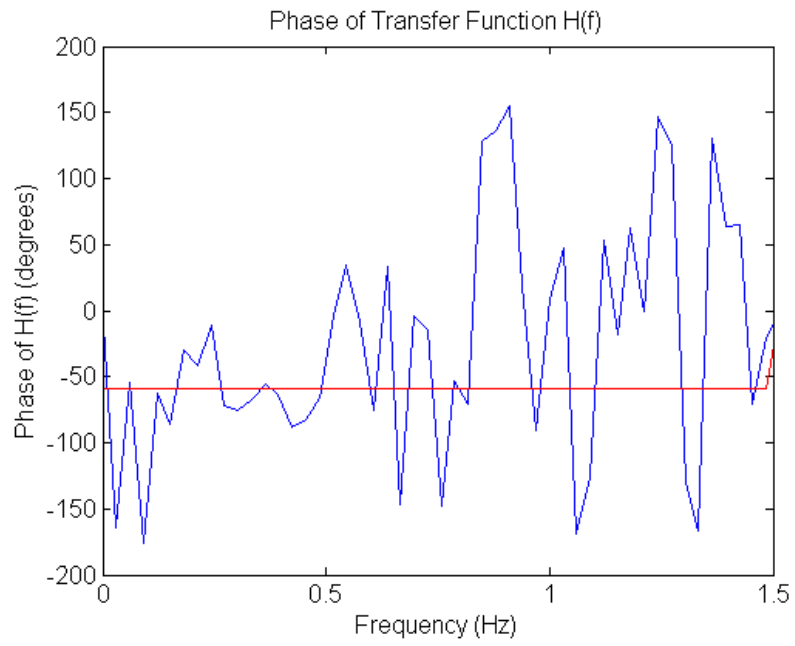


**Figure A.6.** Angle of Transfer function for range of 195 m.

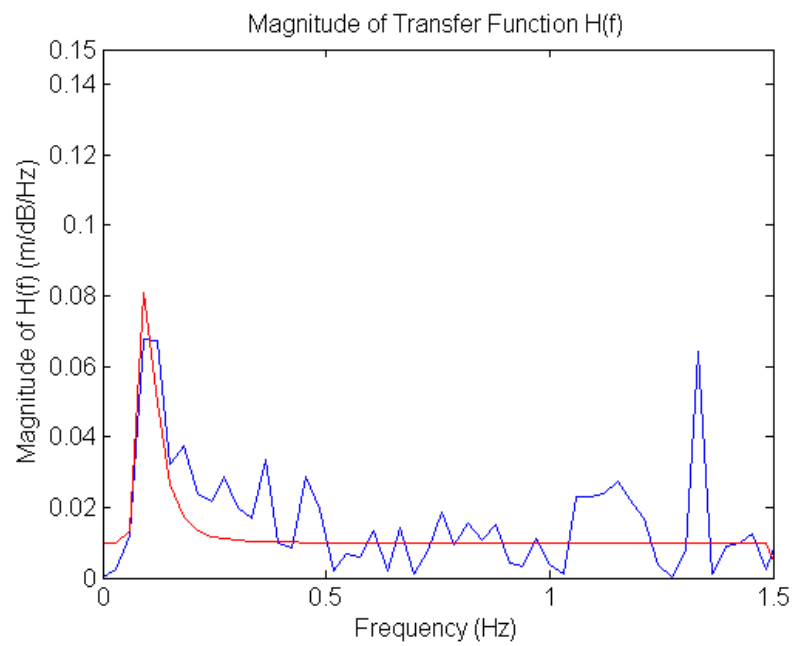


**Figure A.7.** Magnitude of Transfer function for range of 215 m.

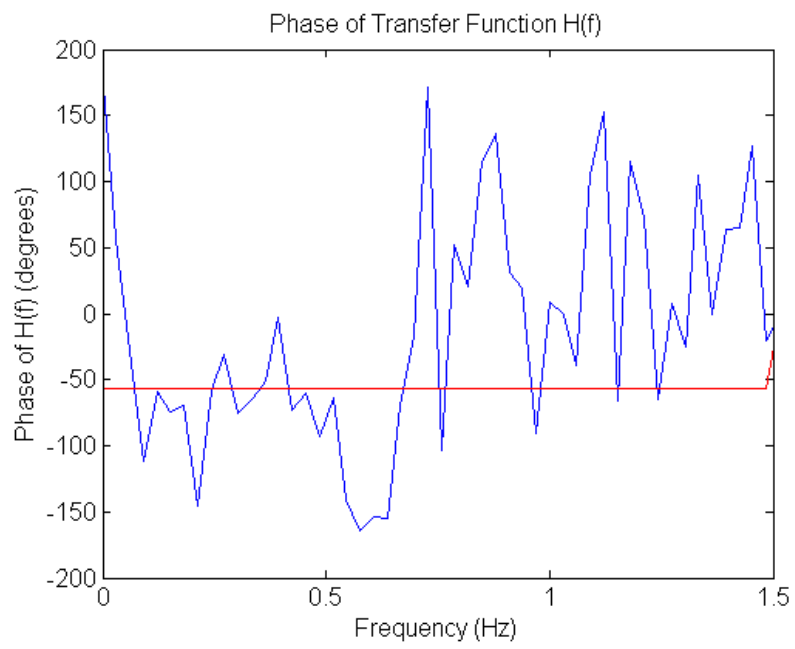


**Figure A.8.** Angle of Transfer function for range of 215 m.

## APPENDIX B

### DATA ALLOCATION IN ENVELOPE IMAGES

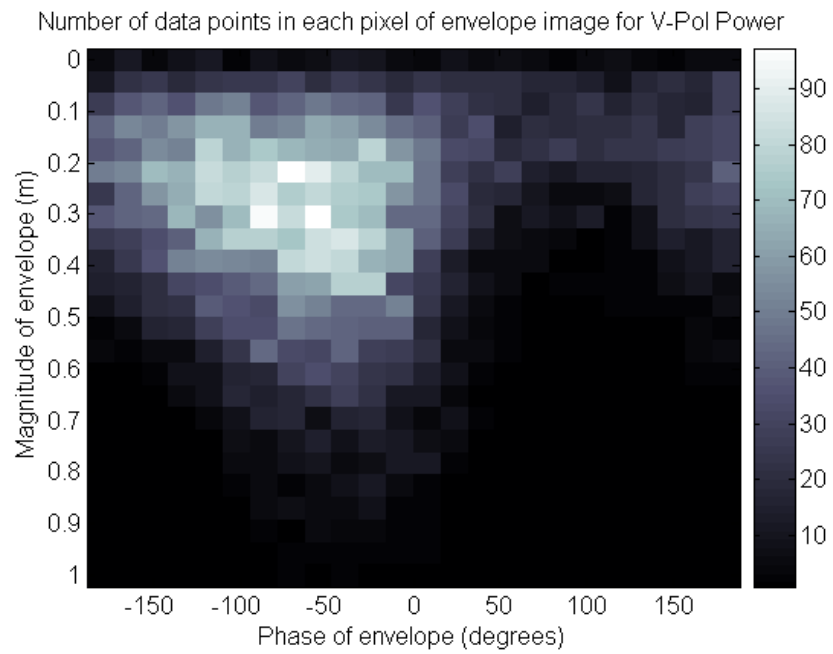


**Figure B.1.** Intensity plot of number of data points in each pixel of Figure 4.10.

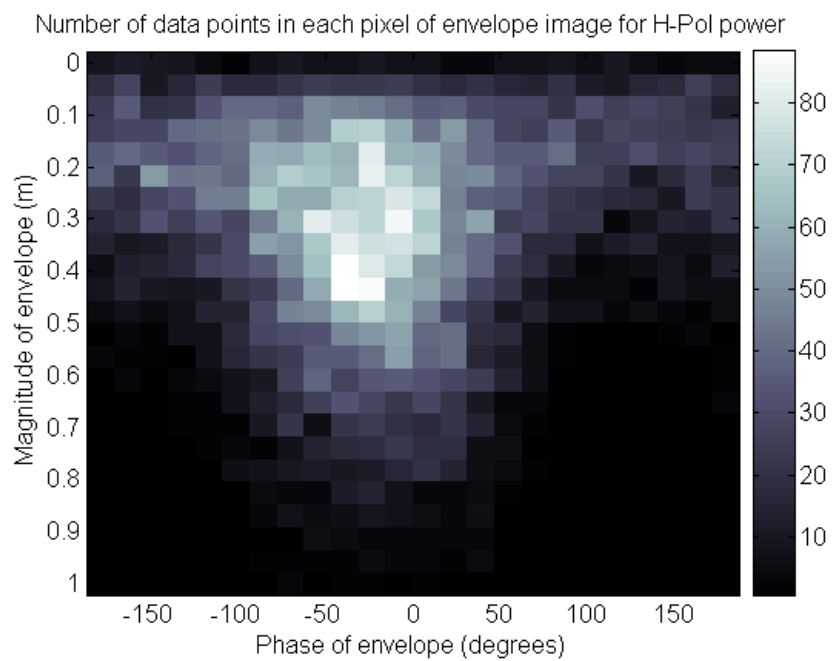


**Figure B.2.** Intensity plot of number of data points in each pixel of Figure 4.11.

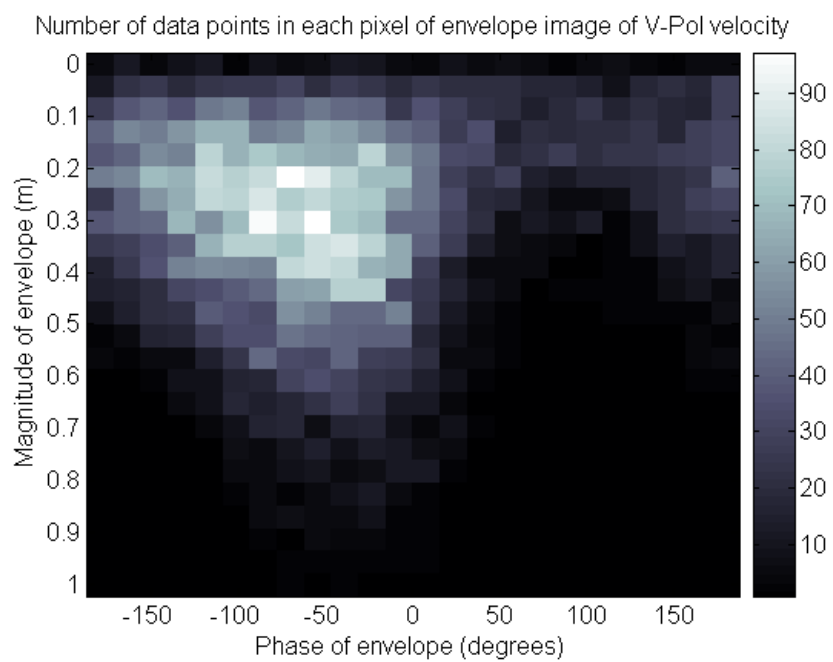


**Figure B.3.** Intensity plot of number of data points in each pixel of Figure 4.12.

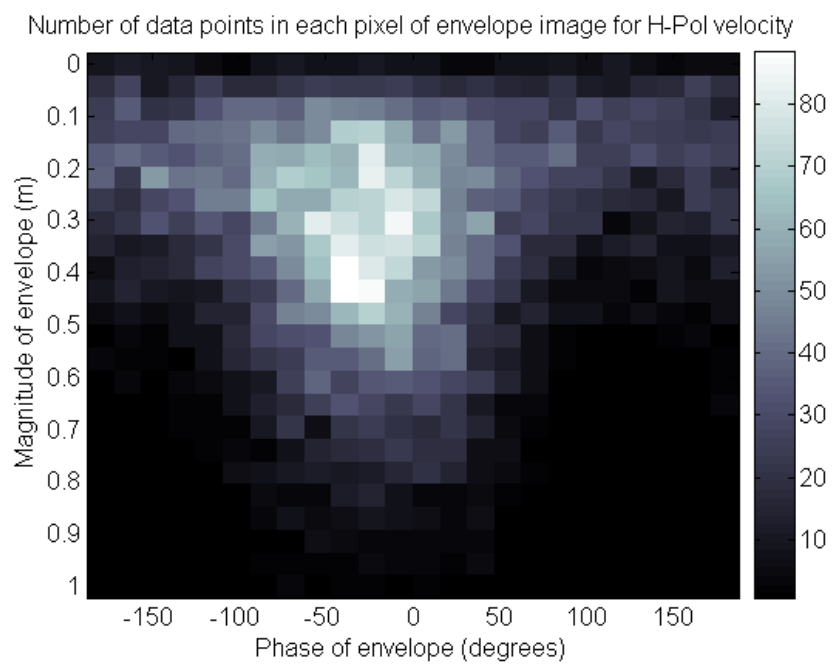


**Figure B.4.** Intensity plot of number of data points in each pixel of Figure 4.13.

## BIBLIOGRAPHY

- [1] Elachi, Charles, and ZYL, Jakob. *Introduction to the Physics and Techniques of Remote Sensing*. John Wiley and sons, 2006.
- [2] Eshbaugh, James V., and Frasier, Stephen J. Measurement of sea surface displacement with interferometric radar. *Journal of Atmospheric and Oceanic Technology* 19, 7 (2002), 1087–1095.
- [3] Farquharson, G., Frasier, S.J., Raubenheimer, B., and Elgar, S. Surf zone surface displacement measurements using interferometric microwave radar. In *Geoscience and Remote Sensing Symposium (IGARSS), 2010 IEEE International* (july 2010), pp. 2428 –2431.
- [4] Frasier, S., and McIntosh, R. Observed wavenumber-frequency properties of microwave backscatter from the ocean surface at near-grazing angles. *J. Geophys. Res.* 101, C8 (1996), 18391–18407.
- [5] Frasier, S.J., Liu, Yong, Moller, D., McIntosh, R.E., and Long, C. Directional ocean wave measurements in a coastal setting using a focused array imaging radar. *Geoscience and Remote Sensing, IEEE Transactions on* 33, 2 (mar 1995), 428 –440.
- [6] Lee, P. H. Y., Barter, J. D., Beach, K. L., Lake, B. M., Rungaldier, H., Thompson, H. R., Wang, L., and Yee, R. What are the mechanisms for non-bragg scattering from water wave surfaces? *Radio Science* 34 (1999).
- [7] Liu, Y., Frasier, S.J., and McIntosh, R.E. Measurement and classification of low-grazing-angle radar sea spikes. *Antennas and Propagation, IEEE Transactions on* 46, 1 (jan 1998), 27 –40.
- [8] Moller, D., Frasier, S., Porter, D., and McIntosh, R. Radar-derived interferometric surface currents and their relationship to subsurface current structure. *J. Geophys. Res.* 103, C6 (1998), 12839–12852.
- [9] Nieto Borge, JosC., Rodriguez, Germn Rodriguez, Hessner, Katrin, and Gonzalez, Paloma Izquierdo. Inversion of marine radar images for surface wave analysis. *Journal of Atmospheric and Oceanic Technology* 21, 8 (2004), 1291–1300.
- [10] Phillips, O. M. The equilibrium range in the spectrum of wind-generated waves. *Journal of Fluid Mechanics* 4, 04 (1958), 426–434.

- [11] Phillips, O.M. *The Dynamics of the Upper Ocean*. Cambridge University Press, 1977.
- [12] Pierson, Willard J, and Moskowitz, Lionel. A proposed spectral form for fully developed wind seas based on the similarity theory of s. a. kitaigorodskii. *Journal of Geophysical Research* 69, 24 (1964), 5181–5190.
- [13] Serafino, F., Lugni, C., and Soldovieri, F. Sea surface topography reconstruction from x-band radar images. *Advances in Geosciences* 19 (2008), 83–86.
- [14] Wetzel, Lewis. On microwave scattering by breaking waves. In *Wave Dynamics and Radio Probing of the Ocean Surface*, O.M. Phillips, Ed. Plenum Publishers, 1986.